Journal Pre-proof

Comparison of Spherical Harmonics Method and Discrete Ordinates Method for Radiative Transfer in a Turbulent Jet Flame

Wenjun Ge, Chloe David, Michael F. Modest, Ramanan Sankaran, Somesh Roy

PII: S0022-4073(22)00394-6
DOI: https://doi.org/10.1016/j.jqsrt.2022.108459
Reference: JQSRT 108459

To appear in: *Journal of Quantitative Spectroscopy & Radiative Transfer*

Received date: 19 August 2022
Revised date: 11 November 2022
Accepted date: 5 December 2022

Please cite this article as: Wenjun Ge, Chloe David, Michael F. Modest, Ramanan Sankaran, Somesh Roy, Comparison of Spherical Harmonics Method and Discrete Ordinates Method for Radiative Transfer in a Turbulent Jet Flame, *Journal of Quantitative Spectroscopy & Radiative Transfer* (2022), doi: https://doi.org/10.1016/j.jqsrt.2022.108459

- Radiation-coupled simulation of a turbulent jet is reported focusing on the performances of PN and DOM
- PN is tested up to the order of 7; DOM is tested up to 8x8 discrete angles
- The convergence mechanisms of PN and DOM with respect to the angular approximation is studied in a 1-D slab with a wide range of optical thicknesses

Comparison of Spherical Harmonics Method and Discrete Ordinates Method for Radiative Transfer in a Turbulent Jet Flame

Wenjun Ge[a,*], Chloe David[b], Michael F. Modest[c], Ramanan Sankaran[a], Somesh Roy[b]

[a]*Computational Sciences and Engineering Division, Oak Ridge National Laboratory, Oak Ridge, TN 37831, USA*
[b]*Opus College of Engineering, Marquette University, Milwaukee, WI 53233, USA*
[c]*School of Engineering, University of California, Merced, CA 95343, USA*

Abstract

In this study, we systematically compared the accuracy and computational cost of two popular solution methods for the radiative transfer equation (RTE): the spherical harmonics method (P_N) and the discrete ordinates method (DOM). We first investigated convergence characteristics of different orders of P_N and DOM in a series of 1D homogeneous configurations with varying optical thicknesses. Both solvers perform better for more optically thick cases. The accuracy of P_N methods increases with its order, N, but the gain in accuracy reduces with the increase in N, i.e., improvement of P_7 over P_5 is less than that of P_3 over P_1. This decreasing trend becomes more prominent as the optical thickness decreases. On the other hand, DOM's accuracy increases almost linearly with the increase in the number of ordinates (or polar angles in this study) in all cases. While comparing the directional profile of radiative intensity, both solvers perform better when the radiative intensity is more isotropic. These solvers were then connected with a full spectrum k-distribution (FSK) spectral model and used to perform radiation-coupled simulations of a turbulent jet flame in an axi-symmetric cylindrical domain. Results are obtained from P_1 to P_7 approximations for P_N, and 2×4, 4×4, 4×8, 8×8 finite angles for DOM are compared with that from an optically thin model, and a reference solution from line-by-line (LBL) photon Monte

*Corresponding author
Email address: gew1@ornl.gov (Wenjun Ge)

Carlo (PMC) method. The choice of radiation solver shows a noticeable impact on the temperature distribution of the flame. The P_N solvers lead to slightly higher radiant fractions and the DOM solvers lead to slightly lower radiant fractions than the PMC benchmark solution. Finally, the computational costs of each of these solvers are also reported and an intermittent evaluation / time blending scheme to improve the computational efficiency of radiation solvers in radiation-coupled simulations are also demonstrated.

Keywords: Radiative transfer, Spherical harmonics method, Discrete ordinates method, Turbulent jet flame

1. Introduction

Thermal radiation is an important mode of heat transfer in combustion [1, 2]. Since radiation is a volumetric phenomenon, its importance in larger combustion systems such as boilers and furnaces is critically important [3, 4]. However, even in small combustion systems, including benchtop combustion experiments, the importance of radiation cannot be neglected. In laboratory-scale laminar flames, thermal radiation affects the flame temperature, the flame speed, and the extinction limits [5, 6]. The radiative heat loss also changes the local temperature distribution, which in turn affects the production of pollutants such as soot and NOx [7, 8]. In turbulent flames the effect of radiation goes beyond the heat loss: The interaction between turbulent structures and radiation, known as turbulence-radiation interaction or TRI, affects the combustion dynamics significantly [9, 10]. Despite of its importance, the modeling of radiative transfer in combustion or relevant conditions are sometimes oversimplified primarily due to the computational complexity associated with radiation modeling.

Radiative intensity is calculated by solving the radiative transfer equation (RTE), which is an integro-differential equation with spectral (i.e., variation of properties with wavelength), spatial, and angular dependencies. The difficulties in modeling radiative transfer in combustion are twofold [11]: a) the highly oscillating spectral dependence of radiative properties of the participating media, and b) the coupled spatial-angular dependence of the RTE.

The spectral dependence of radiative transfer is modeled by spectral models which are broadly classified as gray (i.e., no spectral variation) and nongray models. While gray models are simple and computationally cheap, they are also grossly inaccurate [1]. Spectral models are a field of active research and excellent reviews of some popular spectral models such as weighted sum of grey gas (WSGG), full-spectrum k-distribution (FSK), spectral line weighted-sum-of-gray-gases (SLW) models, ℓ-distribution model, statistical narrow band (SNB) methods, and line-by-line model (LBL) can be found in the literature [12, 13]. The accuracy and complexity of spectral models vary significantly and some researchers have compared the accuracy of different spectral models in various contexts [14, 15].

The solution of the RTE, after accounting for spectral modelling, can be done in either a deterministic or stochastic way. Most deterministic RTE solvers attempt to solve RTE by decoupling the angular dependence of the radiative intensity from its spatial dependence, whereas stochastic RTE solvers often follow a ray-tracing-based Monte Carlo approach. The two most common family of deterministic RTE solvers are the spherical harmonics method and the discrete ordinates method (DOM).

The spherical harmonics method, or the P_N method, approximates the angular distribution by a truncated series of spherical harmonics, where the order N indicates the order of truncation. The spherical harmonics method was first formulated by astrophysicists to describe radiative transfer in stars [16], and was then further studied and developed for neutron-transport theory [17, 18]. Mark [19, 20] and Marshak [21] developed two different approaches to formulate the boundary condition of the P_N method. Arpaci and

Gozum [22] applied the P_3 and P_5 methods to the Bénard problem (natural convection studies between horizontal parallel plates) and found that the results of P_3 and P_5 are increasingly more accurate than P_1, although the accuracy improvement of P_5 is unexpectedly small. Higenyi [23] extended and applied P_N to 1-D problems in cylindrical coordinates and similarly found great improvements for the P_3 approximation over the P_1 approximation and less improvements for P_5. In addition, the P_N approximations in cylindrical and spherical coordinates were shown to be less accurate than in Cartesian coordinates. From these early examples, it can be seen that the convergence characteristics of the P_N series with respect to the truncation order N is problem dependent, even though theoretically, the P_N method converges to the exact solution with an infinitely-large order N. In general, the standard P_N method may suffer from slower convergence when the intensity field is more anisotropic [24]. Detailed derivations of the general 3-D formulation in Cartesian coordinates have been given by Davison [18] and Cheng [25]. However, the number of equations and unknowns as well as the mathematical complexity of the method increases rapidly with the order in multidimensional problems, so that the order of approximation has mostly been limited to P_3 in thermal radiative transfer [26–28] and in neutron transport [29] in real applications. More recent developments of 3-D formulations come from McClarren *et al.* [30] and Modest *et al.* [31–34], independently. McClarren *et al.* [30] developed a semi-implicit linear discontinuous Galerkin method for solving the time-dependent P_N equations with Mark's boundary conditions. Modest and Yang [31, 32] and Modest [33] have developed a general three-dimensional P_N formulation consisting of $N(N+1)/2$ second-order elliptic PDEs and their Marshak's boundary conditions for arbitrary 3-D geometries, which has been implemented in `OpenFOAM`® [35, 36] for radiation-coupled combustion simulations.

The discrete ordinate method is arguably the most popular method for solving RTE. The basic idea of DOM was also first proposed for stellar radiation in the 1960s [37] and was initially adopted for neutron transport [38]. It was later adapted and modified by

numerous researchers for heat transfer [39–41]. In DOM, the directional dependence of the RTE is resolved by performing an angular/directional discretization followed by an integral over the solid angle via numerical quadrature. In simple geometries and without any scattering or reflection effects the DOM results in a series of first-order linear partial differential equation [12]. Because of the simplicity of this system of equations, extensions to higher order approximations of DOM is straightforward. There are several ways in which the angular discretization can be performed for DOM. The traditional approach uses a finite difference scheme, i.e., the RTE is solved over discrete directions spanning the entire 4π solid angle. Instead of discrete directions (i.e., finite differencing), one of the popular variations of DOM uses finite solid angles leading to what is often referred as the finite volume method (FVM) for radiation. This FVM for radiation was first proposed in the 1990s [42–45]. The name *finite volume* method for radiation can be confusing owing to the existence of unrelated spatial finite volume discretization schemes in flow problems. Hence, it has also been referred as Finite Angle Method (FAM) [12]. In this work we use the term FAM instead of FVM to avoid confusion. The FAM-based DOM has been used in complex geometries [46, 47] and in combined heat transfer problems [48, 49]. The finite angle method was found to outperform traditional (i.e., finite difference-based) DOM in various configurations [50–52].

Despite the long existence of different RTE solvers, there have been very few studies that compared them on an equal footing on simple and complex problems. The FAM formulation of DOM was compared with discrete transfer method (DTM) [53] for combustion configurations and FAM was found to perform better than DTM [54, 55]. Mishra *et al.* [56] compared traditional DOM and FAM with DTM for laser transport in participating media and reported comparable results from all. Frank *et al.* [57] compared P_1 method with SP_1 (simplified P_1 [58]) and moment methods for radiation in simple configurations and showed that they all perform comparably. A comparison of P_1 and DOM completed for steam furnace also showed practically no difference between the solvers when used with

a WSGG model [59]. Roy *et al.* [60, 61] compared FAM-based DOM and P_N in frozen field calculations for a turbulent flame and showed that lower-order DOM is slightly more accurate than lower order P_N. Sun *et al.* [49] compared P_1, DOM, and SP_3 in conjugate conduction-radiation problems in 2D and showed that for lower optical thickness DOM performs better than the other two. However, there has not been any systematic study, to our knowledge, that compares these different orders of P_N and DOM either in simple configurations or in coupled combustion simulations. This work attempts to fill that gap in the literature. We present a comparison of P_N ($N = 1, 3, 5, 7$) and FAM (with different angular discretizations) in a simple 1D configuration, where an analytical solution is available, and in a 3D coupled turbulent jet flame simulation. It is noted here that the scope of this work is limited to comparison of radiation models and is not focused on detailed validation of the jet flame simulation, which would require further tweaking and validation of the turbulence model and chemical kinetics model.

The rest of the paper is organized as follows. In Section 2, we describe the basic formulations of the P_N method and DOM used in this study, and their couplings to the reacting flow equations. In this work, we use the FAM formulation for DOM discretization. Hence, unless otherwise specified, for the rest of the document, we will use the name FAM to indicate the FAM-based DOM formulation.

In Section 3.1, the P_N and FAM are applied to a 1D homogeneous problem. The exact solution is obtained for this simple geometry. With this simple example, we look at the different convergence characteristics of the P_N method and FAM for different optical thicknesses. In Section 3.2, a turbulent jet flame is simulated with both P_N and FAM along with an optically thin model and a Monte Carlo model for benchmarking. The computational cost and global characteristics of the flame is compared across all the radiation models. For radiative properties of combustion gases, we use an FSK look-up table [62] as the spectral model with the P_N and FAM in the flame simulations. An accurate line-by-line (LBL) spectral model is used with Monte Carlo RTE solver, while for

the optically thin model, the Planck-Mean absorption coefficient is used.

2. Solution Methods

2.1. Radiative transfer equation

Thermal radiation is heat transfer via electromagnetic wave and therefore occurs at a timescale much faster than that of the reacting flow in conventional combustion systems, so much so that a quasi-steady approximation for radiative transport is adequate. The impact of radiation is included in the energy transport via a source term in the energy conservation equation in combustion systems, which may be written as

$$\frac{\partial \rho h}{\partial t} + \frac{\partial \rho h u_i}{\partial x_i} = -\frac{\partial J_i^h}{\partial x_i} + \frac{Dp}{Dt} + \tau_{ij}\frac{\partial u_j}{\partial x_i} + S_{rad} \,. \tag{1}$$

In Eq. (1), S_{rad} denotes the radiative source term; ρ indicates density; h denotes enthalpy; u_i denotes i^{th} component of velocity vector; J_i^h indicates the effective enthalpy flux; p is the total pressure; τ_{ij} is the stress tensor component, while t and x_i are time and spatial coordinates, respectively. The radiative source term (S_{rad}), which is also the negative of the divergence of the radiative heat flux ($\mathbf{q}$), is the net balance of emission (S_{emi}) and absorption (S_{abs}), i.e.,

$$S_{rad} \equiv -\nabla \cdot \mathbf{q} = S_{emi} + S_{abs} \,, \tag{2}$$

$$S_{emi} = -4\kappa_P \sigma T^4 \,, \tag{3}$$

$$S_{abs} = \int_0^\infty \kappa_\eta G_\eta \mathrm{d}\eta \,, \tag{4}$$

$$G_\eta = \int_{4\pi} I_\eta \mathrm{d}\Omega \,, \tag{5}$$

here I_η is the spectral radiative intensity, and the subscript η denotes wavenumber indicating spectral dependence. κ_η is the absorption coefficient at the wavenumber η, κ_P is the Planck-mean absorption coefficient, and σ is the Stefan-Boltzmann constant. G_η denotes the spectral incident radiation. The spectral radiative intensity (i.e., radiative intensity at wavenumber η), I_η is obtained by solving a quasi-steady spectral radiative transfer

equation, which is a five-dimensional integro-differential equation:

$$\frac{\mathrm{d}I_\eta}{\mathrm{d}s} = \kappa_\eta I_{b\eta} - \kappa_\eta I_\eta - \sigma_{s\eta} I_\eta + \frac{\sigma_{s\eta}}{4\pi}\int_{4\pi} I_\eta \Phi_\eta(\hat{\mathbf{s}}_i, \hat{\mathbf{s}}) d\Omega_i \,. \tag{6}$$

Here radiative intensity $I_\eta(r, \hat{s})$ is the dependent variable; r and $\hat{s}$ are the spatial and directional dimensions of the RTE; σ_η is the scattering coefficients of the medium at the wavenumber η; $I_{b\eta}$ is the blackbody intensity; $\Phi_\eta(\hat{s}_i, \hat{s})$ is the scattering phase function between directions $\hat{s}_i$ and $\hat{s}$; Ω_i is the solid angle. Quantities with a subscript η vary along the electromagnetic spectrum, indicating the spectral nature of the RTE. The left hand side of the equation is the spatial derivative of radiative intensity $I_\eta(r, \hat{s})$, and each term on the right hand side corresponds to an augmentation or attenuation of radiative energy due to emission, absorption, and scattering.

2.2. *Spherical Harmonics Method*

In the spherical harmonics method, also known as the P_N approximation, the radiative intensity is approximated as a finite series of spherical harmonics as

$$I_\eta(r, \hat{s}) = \sum_{n=0}^{N} \sum_{m=-n}^{n} I_n^m(r) Y_n^m(\hat{s}), \tag{7}$$

where $I_n^m(r)$ is the intensity coefficient with respect to the corresponding spherical harmonics basis $Y_n^m(\hat{s})$, so that the spatial and directional dependencies of the intensity $I_\eta(r, \hat{s})$ are decoupled. The spherical harmonics $Y_n^m(\hat{s})$, or $Y_n^m(\psi, \theta)$, satisfy Laplace's equation in spherical coordinates, and their real forms are defined as,

$$Y_n^m(\psi, \theta) = \begin{cases} \cos(m\psi) P_n^m(\cos\theta) & \text{for} \quad m \geqslant 0 \\ \sin(|m|\psi) P_n^m(\cos\theta) & \text{for} \quad m < 0 \end{cases}, \tag{8}$$

where θ and ψ are polar and azimuthal angles, respectively; $P_n^m(\cos\theta)$ are associated Legendre polynomials [63], given by

$$P_n^m(\mu) = (-1)^m \frac{(1-\mu^2)^{|m|/2}}{2^n n!} \frac{\mathrm{d}^{n+|m|}}{\mathrm{d}\mu^{n+|m|}} (\mu^2 - 1)^n \,. \tag{9}$$

Exploiting the orthogonality of the spherical harmonics, one obtains a system of $(N+1)^2$ first-order PDEs for the intensity coefficients. The number of governing equations can be further reduced by eliminating the odd-order intensity coefficients by their relation to the gradients of the even-order ones, which transforms the governing equations from $(N+1)^2$ first-order PDEs into $N(N+1)/2$ second-order elliptic PDEs [31, 32]. For the axi-symmetric flame simulation in this study, the two-dimensional axisymmetric P_N formulation described in [36] is used, which consists of $(N+1)^2/4$ elliptic PDEs, and their corresponding Marshak's boundary conditions.

2.3. Discrete Ordinates Method

In the discrete ordinates method (DOM) following the FAM approach, the directional component of the RTE $\hat{s}$ is discretized into a finite set of N solid angles representing N ordinates. Each ordinate is denoted $\hat{s}_i$ where $i = 1, 2, \ldots, N$ and has a corresponding quadrature weight. Equation (6) is then transformed into a set of N first order PDEs given by

$$\frac{\mathrm{d}I_{i,\eta}}{\mathrm{d}s_i} = \kappa_\eta I_{b\eta} - \kappa_\eta I_{i,\eta} - \sigma_\eta I_{i,\eta} + \frac{\sigma_\eta}{4\pi}\sum_{j=1}^{N} I_{j,\eta}(\hat{s}_j)\Phi_\eta(\hat{s}_j, \hat{s}_i)d\Omega_i \,. \tag{10}$$

This system is solved for N partial intensities $I_{i,\eta}$. Then, numerical quadrature using the partial intensities and the quadrature weights can be employed to approximate the radiative intensity I_η, radiative heat flux $\mathbf{q}$, and incident radiation G. The directional variable $\hat{s}$ is discretized along both the polar (θ) and azimuthal (ϕ) directions. Thus, the discretization that is used in this implementation of FAM is specified by $n_\theta \times n_\phi$ where n_θ is the number of polar angles and n_ϕ is the number of azimuthal angle. The order of accuracy of the FAM is directly related to the total number of ordinates $N = n_\theta \times n_\phi$. The computational expense of FAM is also expected to be correlated with N since N PDEs must be solved.

Usually at least 4 azimuthal angles are used in practice as any less leads to worse results unless the configuration is optically very thick [64]. In the flame simulation of this work, FAM with 2×4, 4×4, 4×8, and 8×8 ordinates are used. Since the most complicated

combustion configuration that is investigated in this work is also rotationally invariant, the axisymmetric formulation of FAM and corresponding rotational invariant boundary conditions are used [65].

2.4. Optically thin and photon Monte Carlo methods

The optically thin (OT) approach and photon Monte Carlo (PMC) approach are the two extremes of RTE solution methods. In OT, the medium is assumed to be optically thin, i.e., it does not absorb any incident radiation and only loses energy by emission. In this case, the RTE does not need to be solved as the radiative source term is simply

$$S_{rad,OT} = -4\kappa_P \sigma T^4 \,. \tag{11}$$

As evident, the OT approach is the simplest, but also the least accurate as it does not capture any reabsorption of radiation.

The PMC method is, on the other hand, the most accurate method to solve RTE. In PMC, the radiative transfer is solved by tracking a large number of radiation rays or photon bundles through the participating medium. Each bundle carries a finite amount of energy which gets absorbed by the medium it passes through. By keeping track of energy deposition by these rays one can resolve the net radiative transfer process. More details of the PMC can be found in the literature [12]. As is with any Monte Carlo approach, PMC require a large number of rays and is computationally very costly. However, with appropriately large number of rays, the PMC solution approaches the exact solution. Hence PMC is usually used as the benchmark solution when exact solution of RTE is not obtainable by analytical means.

2.5. Spectral models

In the flame simulation part of this work (Section 3.2), CO_2, H_2O, and CO are treated as participating species. For radiative properties of these participating species we have used three approaches: a) the Planck-mean gray absorption coefficients [12], b) line-by-line (LBL) model, and c) full-spectrum *k*-distribution (FSK) model.

The LBL model captures the entire thermal radiation spectra of the participating species in terms of individual spectral lines. This leads to several hundreds of thousands to millions of spectral lines for each species. The spectra for the participating species are calculated from the spectroscopic databases [66, 67]. The details of the LBL model used in this work is described in [68].

The LBL calculation requires tremendous amounts of computational resources, which is still impractical for multi-dimensional flame simulations except for the Monte Carlo solvers. To take advantage of the fact that the oscillatory absorption coefficient κ_η has the same value at many different wavenumbers, the *k*-distribution method has been developed to reorder the absorption coefficients into much smoother *k*-distributions. Different variations of the *k*-distribution model exist. Based on the band models, the *k*-distribution can be classified as the narrow band *k*-distribution model [69, 70], the wide band *k*-distribution model [71], or the full-spectrum *k*-distribution model [72]. For nonhomogeneous media, an assumption is needed for the spectral absorption coefficients and it is often assumed that either they obey some scaling law or are well-correlated [72–74] at the application conditions. The original FSCK method [72], or the FSCK-1 method, works well for ideally correlated media, but does not preserve emission in strongly uncorrelated media. To overcome this difficulty, different FSCK methods with emission conservation are formulated, independently by Cai and Modest [73] (FSCK-2), and Solovjov et al. [74] (FSCK-3), which make FSCK applicable to more challenging conditions. Regarding assembling *k*-distribution for mixture, different approaches have been studied, including the superposition method [75], Modest-Riazzi mixing model [76], correlation fitting, or using pre-calculated database [62]. In this study, the full-spectrum correlated-*k*-distribution look-up table [62] based on FSCK-2 [73] is used as the spectral model for flame simulations in this study. The integration of spectral intensities over the whole spectrum is then replaced by the sum of a numerical quadrature with N_g quadrature points with weights w_g,

$$S_{rad} = -\sum^{N_g} w_g k_g (4\pi a_g I_b - G_g) \,, \tag{12}$$

where a_g is the stretching function. Using Gauss quadrature, the FSK is able to reduce the number of required RTE evaluations from over one million required by the LBL method to less than ten [62]. The RTE solvers are connected to the FSK spectral model via a look-up table for radiation-coupled flame simulations. This implementation of FSK look-up table has been shown to produce very accurate results when compared with LBL calculations in simple one-dimensional configurations and in a turbulent jet flame relevant to the one studied in this work [61, 62]. An eight-quadrature-point scheme is used in the flame simulation in this study.

2.6. Radiation-coupled combustion simulation

As demonstrated in Fig. 1, the radiation-coupled flame simulations are two-way coupled, i.e., flow solution serves as an input for radiation calculation whereas radiation provides a source term for flow equations. Turbulence-radiation interaction is not considered in this study because the focus is the performance of RTE solvers, and only mean flow fields and mean radiative heat source are discussed in this study. Both the P_N, and FAM solvers are implemented and coupled to the reacting flow solvers in `OpenFOAM`® software environment. At each time step, the scalars from the flow, species mass fractions ($\mathbf{Y}$), temperature (T), and pressure (P), are passed to the spectral module. In the spectral calculation, k_g, a_g are interpolated from the pre-calculated FSK look-up table. Using them, the governing equations of P_N or FAM are solved for each FSK quadrature point. The integrated radiative heat source, S_{rad}, is then fed back to the energy equation for the next time step.

With radiation-coupled simulation, it can be seen how the accuracy of different RTE solvers affect the resulting flow predictions. From an overall energy balance, it is expected that adding the radiative heat source to the energy equation would result in a flame with lower temperature. The secondary effects (which are due to the temperature changes) are

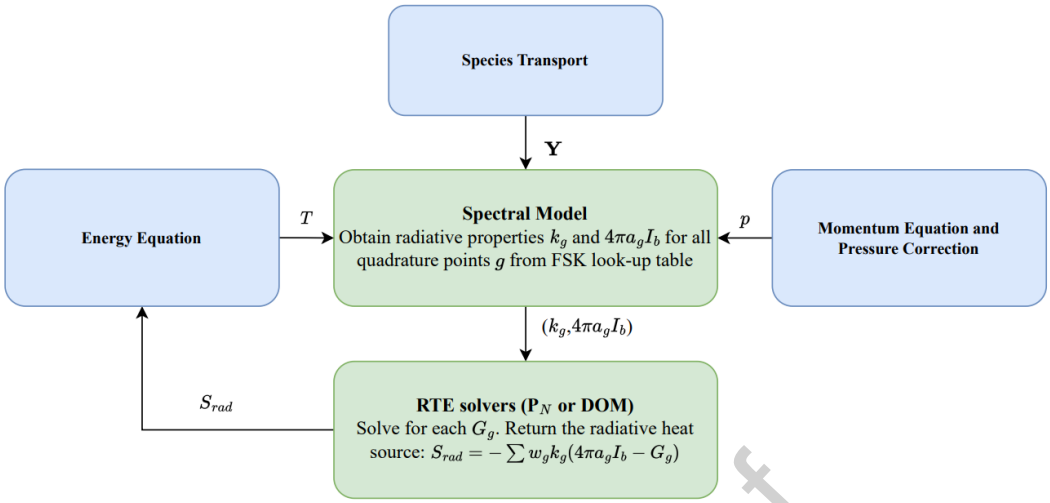

Figure 1: Diagram of the coupling between the flow and radiation.

more difficult to analyze due to the complexity of combustion processes. The temperature changes due to radiation would affect the reaction rates and the resulting combustion products, as well as the thermodynamic properties of the gas mixture, which would in turn return different radiative properties for the RTE solvers.

3. Results and discussions

3.1. Homogeneous medium between two infinitely large plates

The convergence characteristics regarding the angular approximations of the P_N and FAM methods depend on many factors, such as optical thickness, homogeneity of the media, boundary condition, and geometry. A spatially one-dimensional problem is used to verify the P_N and FAM solvers, as well as to study the basic convergence features of both methods. The 1-D problem represents the radiative transfer between two infinitely large parallel plates L distance away from one another, as shown in Fig. 2. An exact solution by direct integration is available for this type of 1-D radiative transfer problems [12] and, therefore, used to evaluate the accuracy of the P_N and FAM methods for different optical thicknesses.

In `OpenFOAM`® 1-D slab problems are solved by treating boundaries at two suppressed

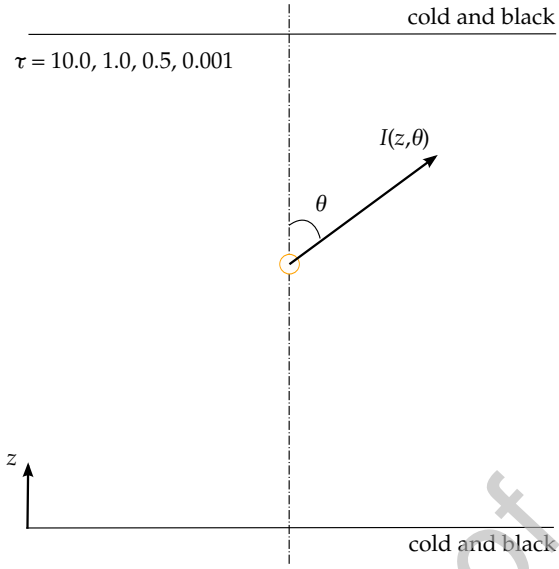

Figure 2: Diagram of the radiative transfer between two infinitely large parallel plates.

dimensions as symmetry/empty boundaries. The lower and upper walls are assumed to be cold and black ($I_w = 0.0, \epsilon = 1.0$). A $1 \times 1 \times 101$ slab is employed and four optical thicknesses ($\tau = 10, 1, 0.5, 0.001$) are selected to test the accuracy of different orders of the P_N methods up to order of 7 and FAM with different numbers of angular discretizations for these optical thicknesses.

The numerical results in terms of normalized quantities are presented in Figs. 3–7 for both the P_N and FAM. Since the medium is homogeneous, the resulting incident radiation, G, radiative heat source, $-\nabla \cdot \mathbf{q}$, and the intensity, I, are normalized by $4\pi I_b$, $4\pi\kappa I_b$ and I_b, respectively. In common applications, only the incident radiation (G) and the radiative heat source ($-\nabla \cdot \mathbf{q}$) are of interest. However, to show the convergence characteristics in terms of angular radiative intensity profiles of the P_N and FAM for different optical thicknesses, the angular distribution of the normalized intensity at the center (i.e., at $\tau/2$) is also presented together with the exact angular distributions of the normalized intensity calculated from direct integration [12]. For the P_N methods, the angular distribution of intensity I is reconstructed by summing up the truncated spherical harmonics expansion, as described by Eqs. (7-9). For FAM, the I is reconstructed from the discrete ordinates and

the corresponding weights.

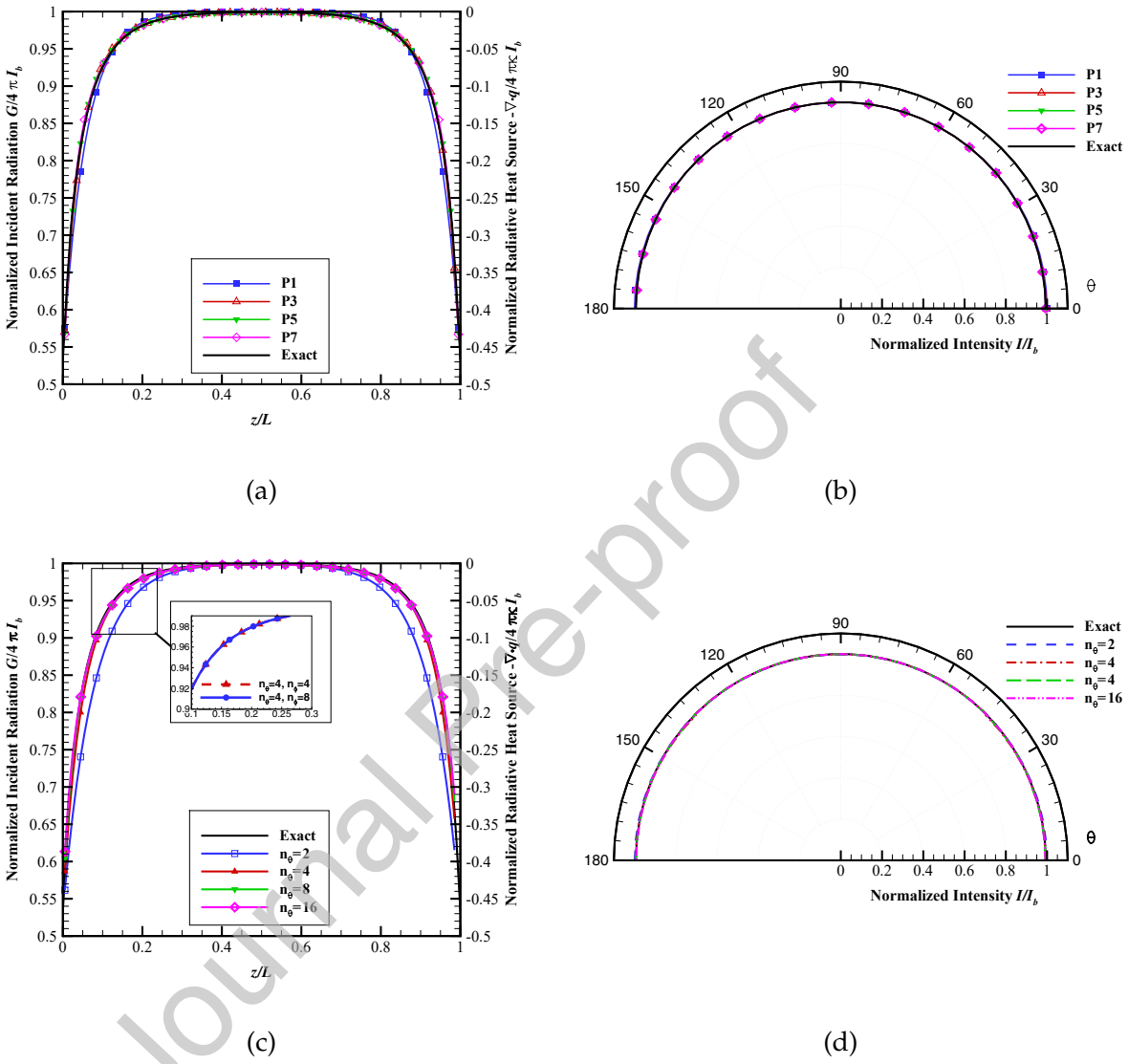

Figure 3: Comparison of numerical solutions from P_N (a)(b) and FAM (c)(d) to the exact solutions for the 1-D slab example with homogeneous medium for optical thickness τ=10; (a)(c) normalized incident radiation $G/4\pi I_b$ and normalized radiative heat source $-\nabla \cdot \mathbf{q}/4\pi\kappa I_b$, and (b)(d) normalized radiative intensity I/I_b.

For the case of $\tau = 10$, which is shown in Fig. 3, all orders of the P_N method give solutions close to the exact solution except that the normalized incident radiation and radiative heat source of P_1 are slightly off next to boundaries (Fig. 3(a)). This is because the angular distributions of the intensities are almost isotropic for optically thick conditions, as shown in Fig. 3(b) for the normalized intensity at the center as a sampling point. On

the FAM side, the results from FAM with more than two polar angles ($n_\theta = 4, 8, 16$) are accurate, but FAM with $n_\theta = 2$ fails to match the exact solution except at the center of the domain. The comparison of FAM with different azimuthal discretizations is also given in the inset of Fig. 3(c). It is confirmed that for this 1-D problem, FAM results only depend on the polar angle as the configuration is azimuthally symmetric. At the optical thickness of 10, the normalized radiative heat source is almost zero close to the center (from z/L=0.3 to 0.7), which reflects the physics that the photons emitted close to the center are absorbed locally so that the net heat exchange at the center is a small portion of the total emission.

There is more energy escaping from the medium to the cold black walls for the case with $\tau = 1$ because the photons can travel ten times longer distances than the case with $\tau = 10$ before getting absorbed, as shown in Fig. 4. The results in Fig. 4(a) show that P_1 incurs large errors in predicting the normalized incident radiation and radiative heat source. P_3 increases the accuracy significantly over P_1 while the results from P_5 and P_7 are very close to the exact solution. The angular distribution of intensity at the center in Fig. 4(b) is anisotropic since the emission path is longer close to $\theta = 90^\circ$ (parallel to the surfaces) than that from $\theta = 0^\circ$ (perpendicular to the surfaces). And P_1 predicts the angular distribution of intensity to be isotropic at the center since the expansion of spherical harmonics of order 1 has only the $I_0^0 Y_0^0$ term at the center (where I_1^m=0). As is shown in Fig. 4(b), increasing the order of P_N consistently improves the accuracy of the P_N method until the intensity predicted by P_7 at the center almost captures the exact angular distribution. The FAM results with $n_\theta = 8$ and 16 show comparable accuracy compared to P_5 and P_7, respectively, while FAM with $n_\theta = 16$ slightly outperform P_7. However, FAM with $n_\theta = 2$ and 4 seem to perform much worse than P_1 and P_3, with $n_\theta = 2$ case predicting an isotropic and smaller angular distribution of intensity at the center.

We further decrease the optical thickness to $\tau = 0.5$. At the optical thickness of 0.5, even P_7 fails to catch the peak of radiative intensity as shown in Fig. 5(b). The angular distribution of intensities at the center predicted by P_1 and FAM with $n_\theta = 2$ are isotropic at

the center, as expected, which fails to capture the anisotropic feature of the exact intensity distribution. The gradually improving results in Fig. 5 for higher order P_N and FAM with more discrete angles are consistently closer to the exact solution. Oscillations in the angular distributions are observed for the high-order P_N methods in Fig. 5(b). The high order spherical harmonics Y_n^m represent high-frequency bases of a function, and therefore, higher-order spherical harmonics expansions are able to closely approximate the exact anisotropic angular distributions but also introduces oscillations to the solution with regard to angular distributions of intensity.

The root mean squared (rms) relative error of the $\tau = 1$ and 0.5 cases for both methods are shown in Fig. 6. The rms relative error is calculated as

$$\varepsilon = \sqrt{\frac{1}{M}\sum_{i=1}^{M}\left(\frac{\tilde{G}_i - G_i}{G_i}\right)^2}, \tag{13}$$

where M is the number of grid points where radiation is evaluated, $\tilde{G}$ is the approximate solution, and G is the exact solution. Both the P_N and FAM solvers perform better in the optically thicker case ($\tau = 1$) than in the $\tau = 0.5$ case, as expected. The rms relative errors of P_1 and P_3 are smaller than the errors from FAM with $n_\theta = 2$ and 4, respectively. P_5 shows a comparable performance to FAM with $n_\theta = 8$, with much closer rms relative errors between the two solvers. FAM with $n_\theta = 16$ outperforms P_7, with a much larger margin for the optically thinner case (τ=0.5). Performances of the P_N and FAM essentially depend on the number of equations that need to be solved. For a general 3-D problem, $N(N+1)/2$ equations need to be solved for the P_N method and $n_\theta \times n_\phi$ equations need to be solved for the FAM. For this 1-D case, the numbers of equations required can be reduced to n_θ for FAM, and $(N+1)/2$ for P_N. Limited to this example, it can be seen that low-order P_N methods performs better than DOM with less discrete ordinates, but high-order P_N gradually loses its advantages over FAM with more discrete ordinates.

Figure 7 shows the results for the condition of an optically thin case with $\tau = 0.001$. Both P_N method and FAM show some relative error for incident radiation under the optically

thin condition due to the small value of G in this case. The error reduction using higher order P_N becomes much less effective than in the $\tau = 0.5$ case. As shown in Fig. 7(a) and (b), the improvements from applying a higher order P_N become less and less with the increase in order. It implies that a much higher order of P_N is necessary to predict the correct incident radiation for such an optically thin case. Even though FAM also fails to predict the correct incident radiation, as shown in Fig. 7(c) and (d), the improvements from adding more ordinates seem to be linear. This is due to the highly anisotropic angular profiles of the intensity, which are shown in Fig. 7(b) and (d). Since discrete ordinates follow along specific solid angles (some of which will align with the anisotropic intensity), FAM results seem to improve faster than P_N with an increase of respective orders in case of highly anisotropic profiles such as this case. It is important to point out that the radiative heat source before normalization is what will eventually matter, and if one looks at the total scale of energy absorbed in Fig. 7(a), which is around 0.2-0.4% of the emitted energy, the error of the P_N method actually can be safely ignored. Even an optically thin solution will be sufficient for this homogeneous optically thin example. However, the argument that the errors from radiation calculation is not relevant in optically thin conditions is only valid for this type of simple homogeneous cases. For non-homogeneous scenarios, which is usually the case in combustion simulations, the optical thickness significantly vary locally. It is, therefore, much more difficult to predict the performances of the RTE solvers in actual combustion simulation based on just 1-D calculation results.

3.2. Turbulent flame

3.2.1. Target flame

Sandia Flame D is a turbulent piloted jet flame [77] with a Reynolds number of Re_D=22,400. The fuel from the main jet is a mixture of methane and air with a ratio of 1:3 by volume. The main jet with a diameter of $d_j = 7.2$ mm at the center is surrounded by an annular pilot with a diameter of $2.62d_j$ to stabilize the main jet. The precise and careful measurement of Sandia Flame D provided a series of high quality experimental data that makes it a standard benchmark of a turbulent jet flame to validate combustion

Table 1: Sizes of the main jet, and the pilot and the inlet velocities for the original and scaled Sandia Flame D

	Sandia Flame D		Sandia Flame D×4	
	d (mm)	u (m/s)	d (mm)	u (m/s)
main jet	7.2	49.89	28.8	12.4725
pilot	18.864	10.57	75.456	2.6425
co-flow	258.2	0.90	1032.8	0.2250

models.

The effects of radiative transfer for the simulation of Sandia Flame D have been studied by Li [78], and Pal [79] previously. The importance of radiation and its interaction with turbulence (TRI) have been established by comparing the simulation results and the experimental measurements. Pal [79] also found that different spectral models and RTE solvers yield similar results because of the relatively small size of Sandia Flame D. For this case, the P_1 RTE solver with a FSK spectral model is sufficient for the radiation calculations (though the small differences in predicted temperature resulted in totally different predictions of NO) [79]. Since the size of turbulent jet flames in real applications tends to be much larger, Sandia Flame D was numerically scaled four times (Sandia Flame D×4) to study the effects of radiation for thicker turbulent jet flames [78, 79]. This scaling is done in such a way that the diameter of the main jet and the outer diameter of the pilot are quadrupled while decreasing the exit velocity of the mixture out of the jet and pilot to keep the Reynolds number unchanged. In this work, we use the scaled up Sandia Flame D×4 as our target flame. The geometric sizes of the main jet and the pilot and the inlet velocities of the original Sandia Flame D and Sandia Flame D×4 are shown in Table 1. The co-flow represents the environmental air entering the wind tunnel.

3.2.2. Problem setup

In this study, a 10° wedge shaped grid consisting of 3325 cells (35 cells along the radial direction, or r-axis and 95 cells along the axial direction, or z-axis) is employed for radiation-coupled reacting Reynolds-averaged simulation (RAS). The full size of the computational domain is 0.516 m × 2.88 m and the mesh is optimized to have a finer mesh

close to the jet to resolve the large local gradients there, and coarser in the co-flow region and downstream of the flame to save computational time. The inlet boundary conditions for temperature, velocity and mass fractions of gases are listed in Table 2. Since the P_N formulation is not able to handle any computational cell with zero absorption coefficient, a minimum value of 0.001 m^{-1} for absorption coefficient is used in simulation. For the radiative transfer, the outside boundaries are treated as cold and black and the top and bottom walls are treated as symmetry/specular reflection walls.

Table 2: Inlet boundary conditions of Sandia Flame D×4

	main jet	pilot	co-flow
T (K)	293	1880	291
u (m/s)	12.4725	2.6425	0.2250
Y_{CH_4}	0.15605	0.0	0.0
Y_{O_2}	0.1962	0.054	0.23113
Y_{H_2O}	0.0	0.0942	0.00581
Y_{CO_2}	0.00045	0.1098	0.00055
Y_{N_2}	0.6473	0.7377762	0.76251
Y_{CO}	0.0	0.00407	0.0
Y_{H_2}	0.0	0.000129	0.0
Y_H	0.0	0.0000248	0.0

In this study, a pressure-based algorithm named PIMPLE or merged PISO (Pressure Implicit with Splitting of Operator)–SIMPLE (Semi-Implicit Method for Pressure Linked Equations) algorithm [80] in `OpenFOAM`® 2.2.x, is employed to resolve the coupling between pressure and velocity. Since the maximum velocity of the reacting flow in the Sandia Flame D×4 is much smaller than a Mach number of 0.3, compressibility of the gases can be neglected, and therefore, PIMPLE is suitable for the flow simulation of Sandia Flame D×4. A standard two-equation $k-\epsilon$ model is employed as the turbulence model. The pressure-coupled momentum equation, the energy equation, species transport equations, and $k-\epsilon$ equations along with the chemical kinetics equations are iterated in sequence to calculate the flow fields of the flame. In the $k-\epsilon$ model, the $C_{\epsilon 1}$ was increased to 1.55 for a better representation of the turbulent flow field. A 49 species and 277 reactions chemical reaction mechanism for methane, GRI–Mech 2.11 [81], is employed as chemistry

mechanism and the SIBS (Semi-Implicit Bulirsch Stoer) ODE solver [82] is used to solve the chemical reaction equations. The PaSR (Partially Stirred Reactor) model [83] is employed for turbulence-chemistry closure. PaSR is a 0-D reactor inside which the gas is partially mixed representing nonhomogeneous thermo-chemical states that evolve under chemical reaction and turbulent mixing.

Radiation models are computationally costly. To save computational time, the simulation is run in steps in the following manner. The simulation starts with no-radiation reacting flow. After running the no-radiation reacting flow for 2.2 s (about 9.5 flow-through times of the main jet or 2 flow-through times of the pilot), radiation models are activated. The radiation-coupled reacting flow keeps running for another 1.1 s until a time of 3.3 s. A constant time step of 8×10^{-6} s is used starting from 0 s to the end (3.3 s). Thus, from 2.2 s to 3.3 s, during which time the radiation models are considered, there are a total of 137,500 time steps. One advantage of the FAM and P_N methods in radiation-coupled combustion simulations is that they are able to use results of previous time steps as initial values for iterations at the next time step, which reduces the computational cost of iterations required for FAM and P_N methods. The governing equations for FAM are not coupled with one another for non-scattering media so that the benefit of good initial guess is limited. For the high-order P_N methods, since the governing equations are strongly coupled, storing the results from previous time steps significantly reduces the total numbers of iterations required. The computational time for the RTE solvers can be further improved by reducing the frequency of radiation evaluations for the radiation-coupled simulation. This is based on the fact that, in the multi-scale simulation of combustion, the time step is often determined by chemical models and, therefore, the change of the flow field may be small between time steps leading to only minor changes in the distribution of S_{rad} (or $\nabla \cdot \mathbf{q}$). Therefore, four different frequencies are chosen for solving radiation, i.e., the P_N and FAM solvers are only invoked every 1/10/100/250 time steps. This multiscale feature of radiation-coupled simulation can also be taken advantage of by a time-blending scheme

for the PMC solver. Time-blending reduces the number of photon bundles required to be tracked at each time step by retaining the history of previous time steps. With time-blending, a relatively small number of photons at each time step is traced, which gives the radiative heat source $(\nabla \cdot \mathbf{q})^{(k)}$, and then to blend with previous results with different weights to calculate the averaged radiative heat source $(\overline{\nabla \cdot \mathbf{q}})^{(k)}$ for time step k. In this study, the PMC calculation employs 5,000 photon bundles per time step with a recursive time-blending scheme, as given by:

$$(\overline{\nabla \cdot \mathbf{q}})^{(k)} = (1-\alpha)(\nabla \cdot \mathbf{q})^{(k)} + \alpha(\overline{\nabla \cdot \mathbf{q}})^{(k-1)} \quad \text{with} \quad (\overline{\nabla \cdot \mathbf{q}})^{(0)} = 0,\ k = 1, 2, 3, \cdots \tag{14}$$

with a blending factor $\alpha = 0.98$. This scheme is equivalent to employing about 1.25 million photon bundles for every 250 time steps (the contribution from the radiation field 250 time steps ago is $0.02 \times (0.98)^{250} = 1.28 \times 10^{-4}$). Another scheme with the same blending factor but with 10,000 photon bundles per time step is also used as an accuracy validation for the former one. All computations are performed on 12 Intel® Xeon® X7460 (2.66 GHz) processors. Simple domain decomposition into blocks with same number of cells along the axial direction is employed.

3.2.3. Results

The effects of radiation on the temperature predicted by different RTE solvers in the case of Sandia Flame D×4 are demonstrated in Fig. 8 in a 2-D contour plot followed by Fig. 9 showing centerline profiles. The P_N/FAM+FSK results with different solving frequencies are found to be almost the same and are not reproduced here for brevity. The PMC+LBL results with different photon bundles per time step are also found to be very close to each other. Hence, only one PMC+LBL result is shown as the reference solution to be compared with. The profiles of radiative heat source and standard deviations of the PMC+LBL method (with 5,000 photon bundles per time step) at three axial locations are shown in Fig. 10, as well, for reference. The standard deviation, shown as the error bar in PMC results, is obtained by splitting the photon bundles in each time step into 10

sampling groups.

Radiation and reacting flow are fully coupled in the simulations, so that different radiation models result in different radiative heat sources and, therefore, different temperature distributions, which in turn further lead to different chemical reaction rates and species concentrations. As expected, adding radiative transfer cools down the flame. It can be seen that for Sandia Flame D×4, the choice of radiation model plays a very important role. Totally ignoring radiation introduces the largest error by over-predicting the flame temperature. The OT approximation ignores absorption and predicts the lowest temperature distribution; the P_N+FSK, FAM+FSK, and PMC+LBL predict considerably higher temperatures than the OT due to self-absorption. All FAM+FSK results are found to be very close to the PMC+LBL results, and only the temperature contours predicted from $FAM_{4\times4}$+FSK and $FAM_{8\times8}$+FSK are shown in Fig. 8 for reference. The small differences between the results predicted by $FAM_{8\times8}$+FSK and PMC+LBL are believed to be partly due to the errors of FSK. P_1+FSK performs much better than OT, but it still under-predicts the flame temperatures compared with the results from high-order P_N+FSK, FAM+FSK and PMC+LBL. P_3 only slightly improves the temperature profile compared with P_1 while P_5 and P_7 are very close to P_3 results. The temperature profiles predicted by high-order P_N methods are still quite different from the FAM and PMC results. The overall accuracy of the P_N method in the axi-symmetric flame simulation seem to be worse than they are in the 1-D slab case, when compared to the corresponding FAM results, but it is consistent with the previous findings comparing P_N in Cartesian and cylindrical geometries [23].

Peak temperatures along the centerline, $T_{p,c}$, predicted from different solvers as shown in Fig. 9, are summarized in Table 3. By comparing the peak temperatures, one can observe a decrease of temperature when employing different radiation models. The emission-only OT model predicts a drop of peak temperature of 520 K; the PMC+LBL predicts a drop of 329 K; the FAM+FSK predict the temperature drops of 330 K, 338 K, 350 K and 353 K with an increase in number of discrete ordinates; P_1+FSK predicts a drop of 408 K, while the

high-order P_N+FSK models predict a peak temperature drop of around 386 K.

Table 3: The peak temperatures along the centerline $T_{p,c}$ predicted from different solvers at 3.3 s

Radiation Solvers	$T_{p,c}$ (K)	$\Delta T_{p,c}$ (K)	%
No Rad.	2074	/	/
OT	1554	-520	-25.1
P1+FSK	1666	-408	-19.7
P3+FSK	1683	-391	-18.8
P5+FSK	1688	-386	-18.6
P7+FSK	1689	-385	-18.6
FAM 2×4	1744	-330	-15.9
FAM 4×4	1736	-338	-16.3
FAM 4×8	1724	-350	-16.9
FAM 8×8	1721	-353	-17.0
PMC+LBL	1745	-329	-15.9

The radial distributions of two scalars, i.e., temperature (T) and mass fraction of nitrogen monoxide (Y_{NO}) at three axial locations $z/d_j = 15$, $z/d_j = 30$ and $z/d_j = 45$ are shown in Figs. 11 and 12, respectively. These two plots show the flame structure and distribution of the pollutant NO. Formation of NO is very sensitive to the local temperature, hence profiles Y_{NO} provide an indication how the radiation calculation affects the chemical reactions indirectly via its impact on temperature distribution. The radial profiles of both scalars predicted by FAM+FSK are very close to those from the PMC+LBL. For the temperature predictions, at upstream locations of $z/d_j = 15$ and 30, P_1+FSK results are shown to be already very close to PMC+LBL results, while at the downstream location of $z/d_j = 45$, the errors of P_N methods are larger. As the NO production is very sensitive to temperature, larger differences in NO profiles can be seen between different radiation solvers. The P_N+FSK solvers underpredict the Y_{NO} by about 20% at the peak due to the slight underprediction of the temperature. Although FAM+FSK results, except the lowest resolution one, predict accurate NO mass fractions (Fig. 12) at the the center and close to the peaks, there are discrepancies between FAM+FSK and PMC+LBL results at $r/d_j > 2$ at $z/d_j = 15$ in Fig. 12(a), and $r/d_j > 2.6$ at $z/d_j = 30$ in Fig. 12(b). Instead, the FAM+FSK results are found to be close to the P_N+FSK results at these locations.

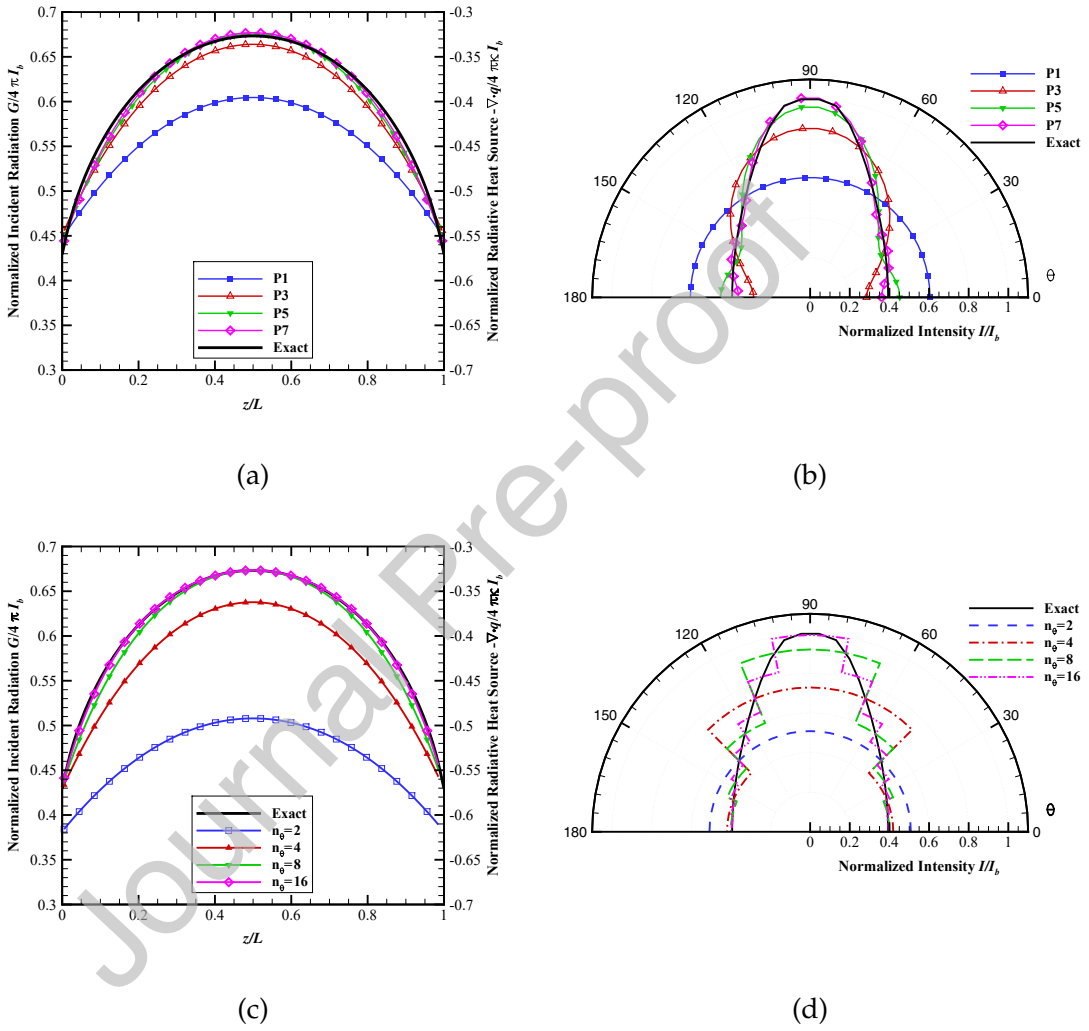

Figure 4: Comparison of numerical solutions from P_N (a)(b) and FAM (c)(d) to the exact solutions for the 1-D slab example with homogeneous medium for optical thickness τ=1; (a)(c) normalized incident radiation $G/4\pi I_b$ and normalized radiative heat source $-\nabla\cdot\mathbf{q}/4\pi\kappa I_b$, and (b)(d) normalized radiative intensity I/I_b.

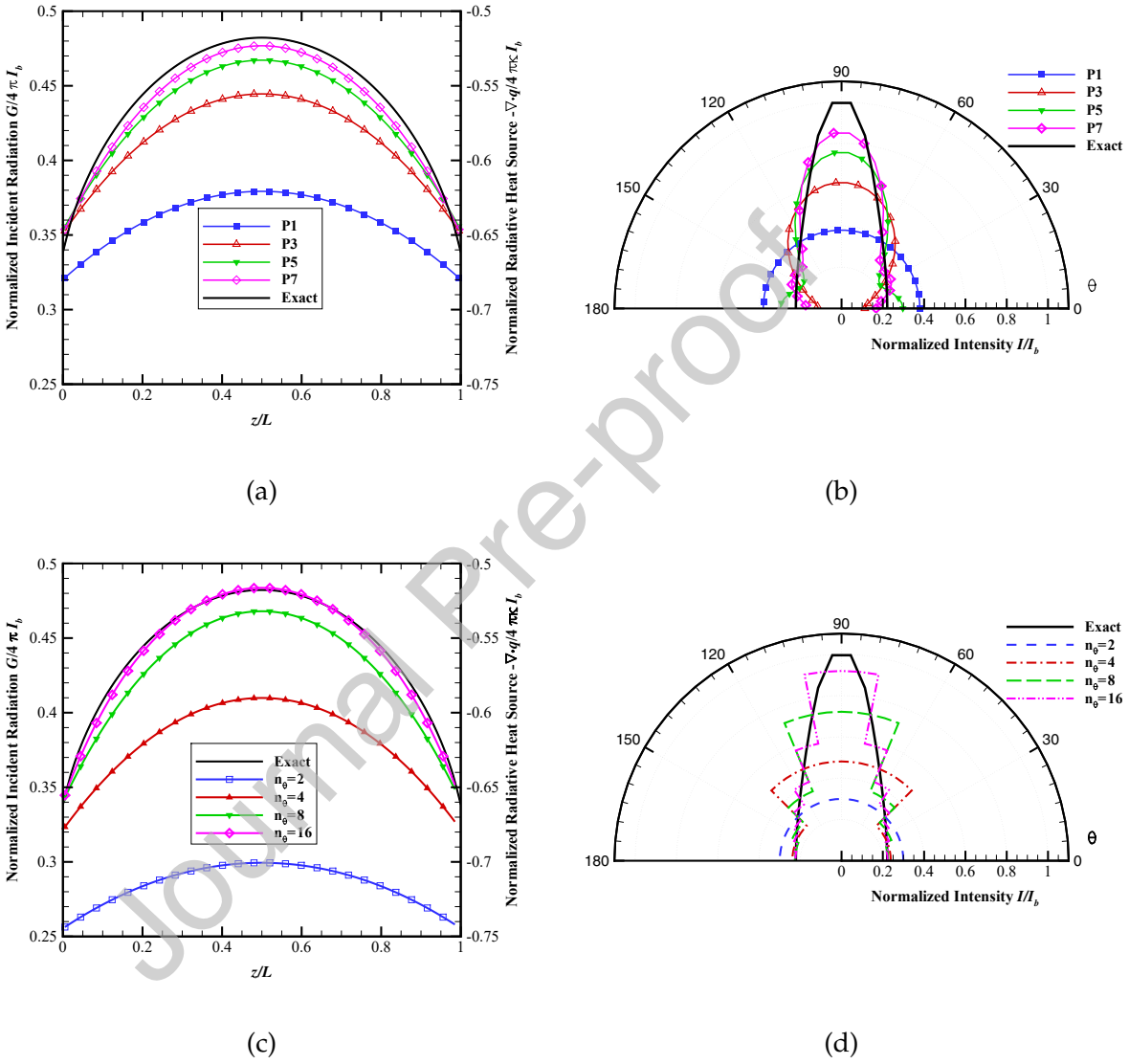

Figure 5: Comparison of numerical solutions from P_N (a)(b) and FAM (c)(d) to the exact solutions for the 1-D slab example with homogeneous medium for optical thickness τ=0.5; (a)(c) normalized incident radiation $G/4\pi I_b$ and normalized radiative heat source $-\nabla \cdot \mathbf{q}/4\pi\kappa I_b$, and (b)(d) normalized radiative intensity I/I_b.

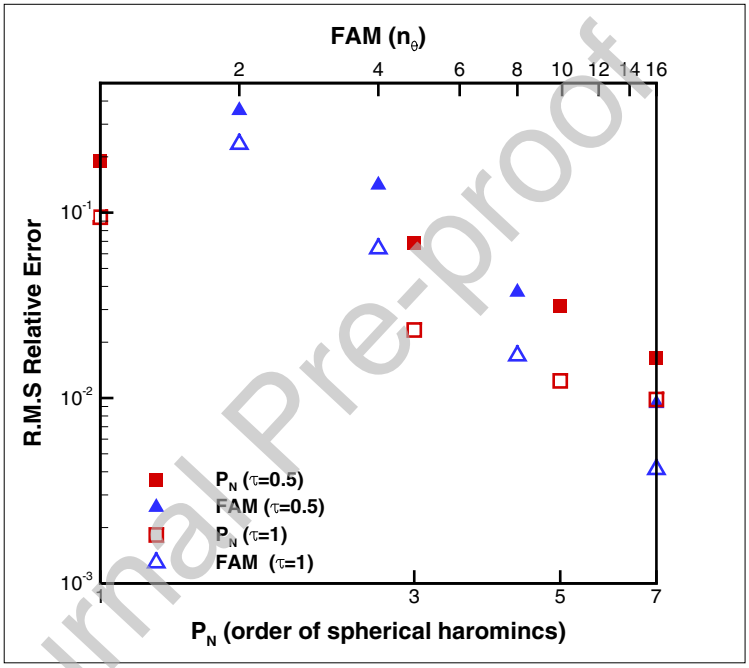

Figure 6: Order of convergence in $\tau = 0.5$ and $\tau = 1$ cases with respect to the order of spherical harmonics method (P_N, lower x-axis) or number of polar angles (FAM, upper x-axis). The symbols represent rms relative error in G from each solution.

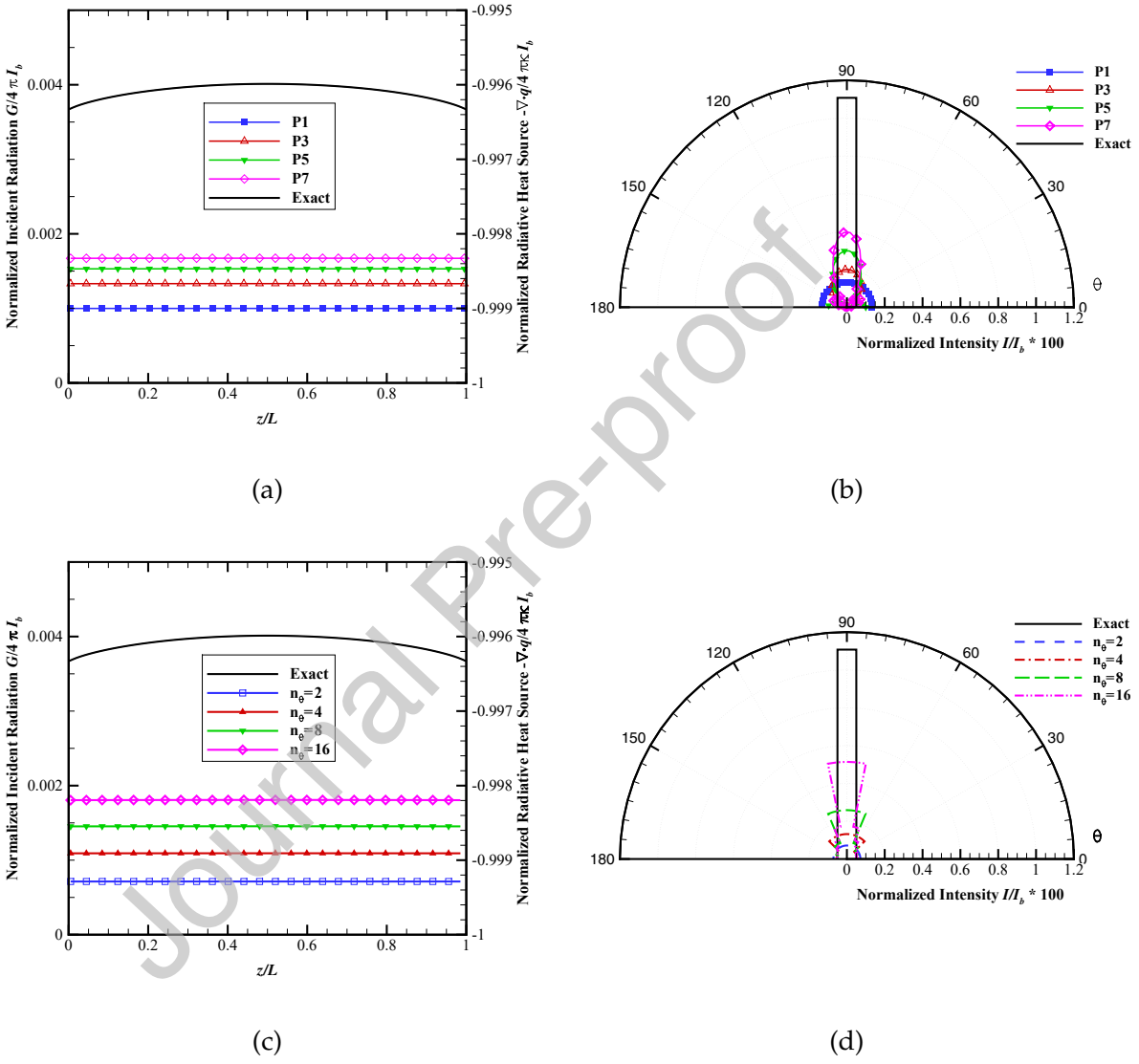

Figure 7: Comparison of numerical solutions from P_N (a)(b) and FAM (c)(d) to the exact solutions for the 1-D slab example with homogeneous medium for optical thickness τ=0.001; (a)(c) normalized incident radiation $G/4\pi I_b$ and normalized radiative heat source $-\nabla \cdot \mathbf{q}/4\pi\kappa I_b$, and (b)(d) normalized radiative intensity I/I_b.

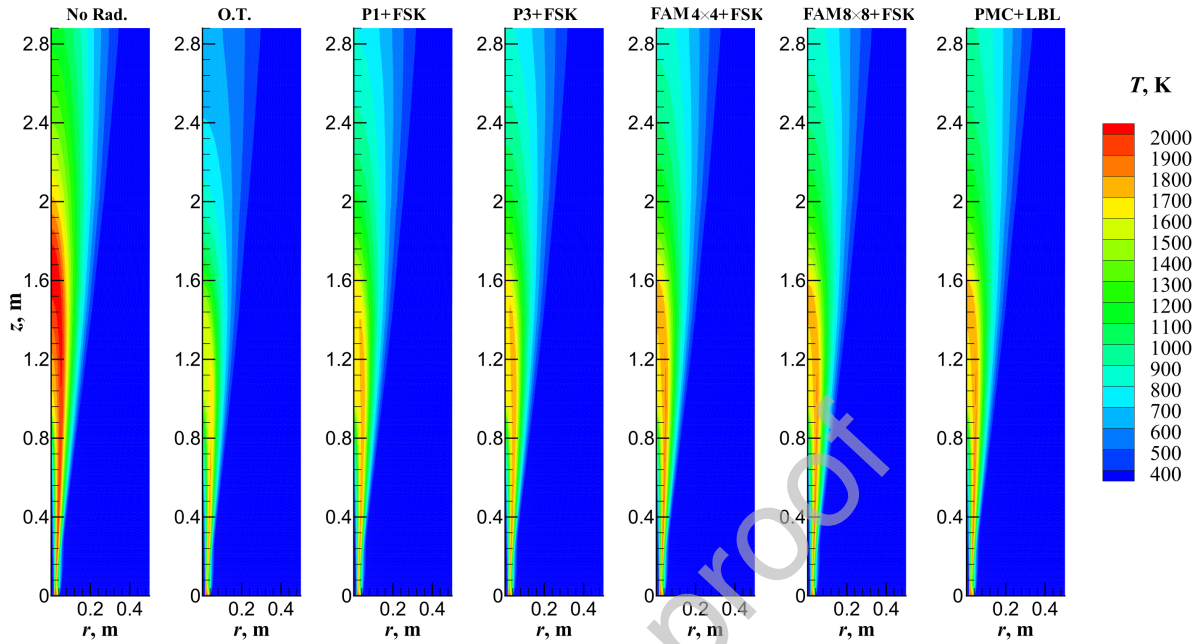

Figure 8: Effects of different RTE solvers on temperature distribution after two flow-through time (at 3.3 s). The movie of the baseline flame simulation without radiation model is provided in the Supplementary Materials.

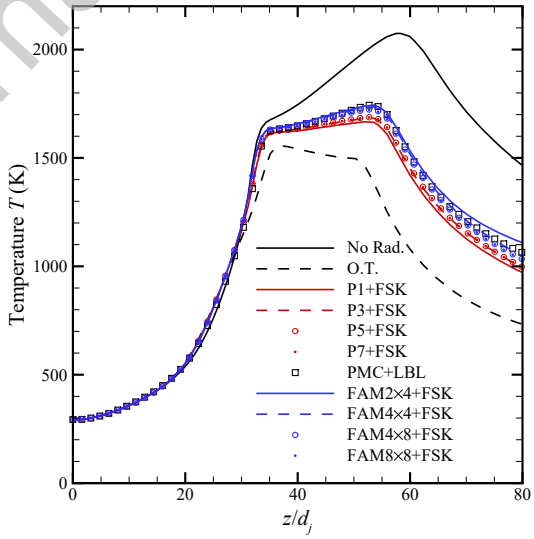

Figure 9: Centerline profiles of temperature.

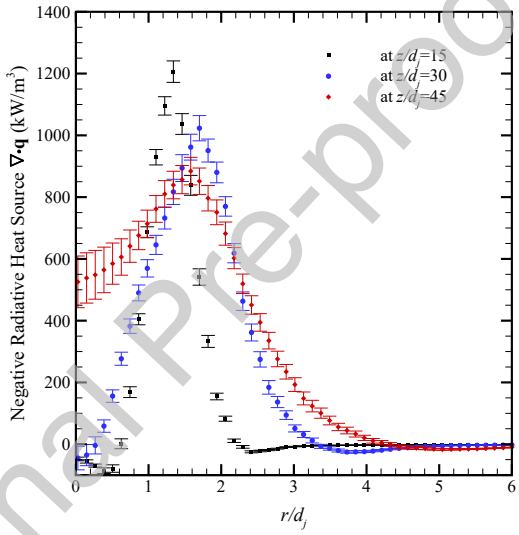

Figure 10: Negative radiative heat source $\nabla \cdot \mathbf{q}$ and the corresponding standard deviation from the PMC+LBL solver at three axial locations ($z/d_j = 15, 30, 45$).

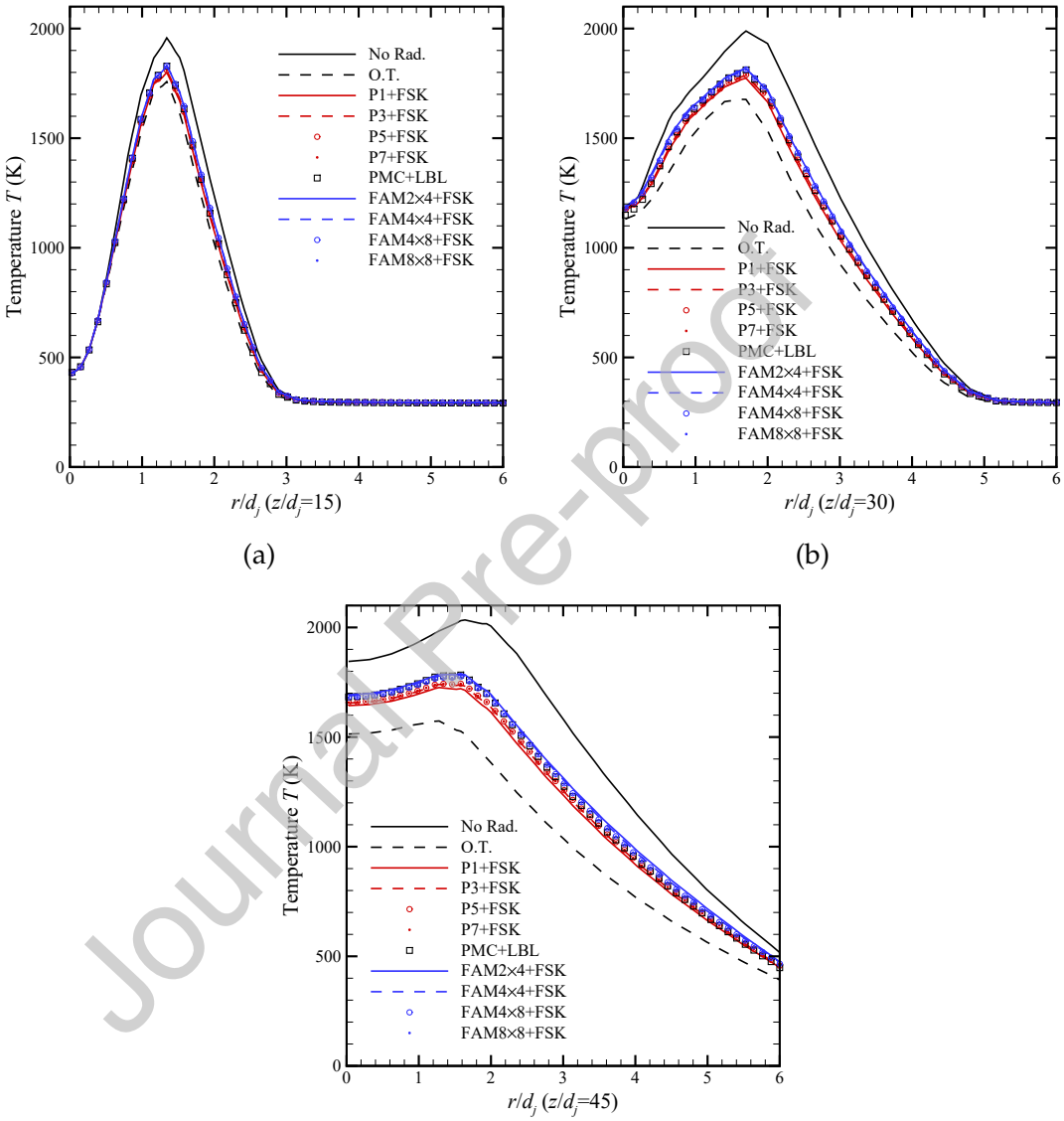

Figure 11: Temperature profiles at different axial locations: (a) $z/d_j = 15$, (b) $z/d_j = 30$ and (c) $z/d_j = 45$.

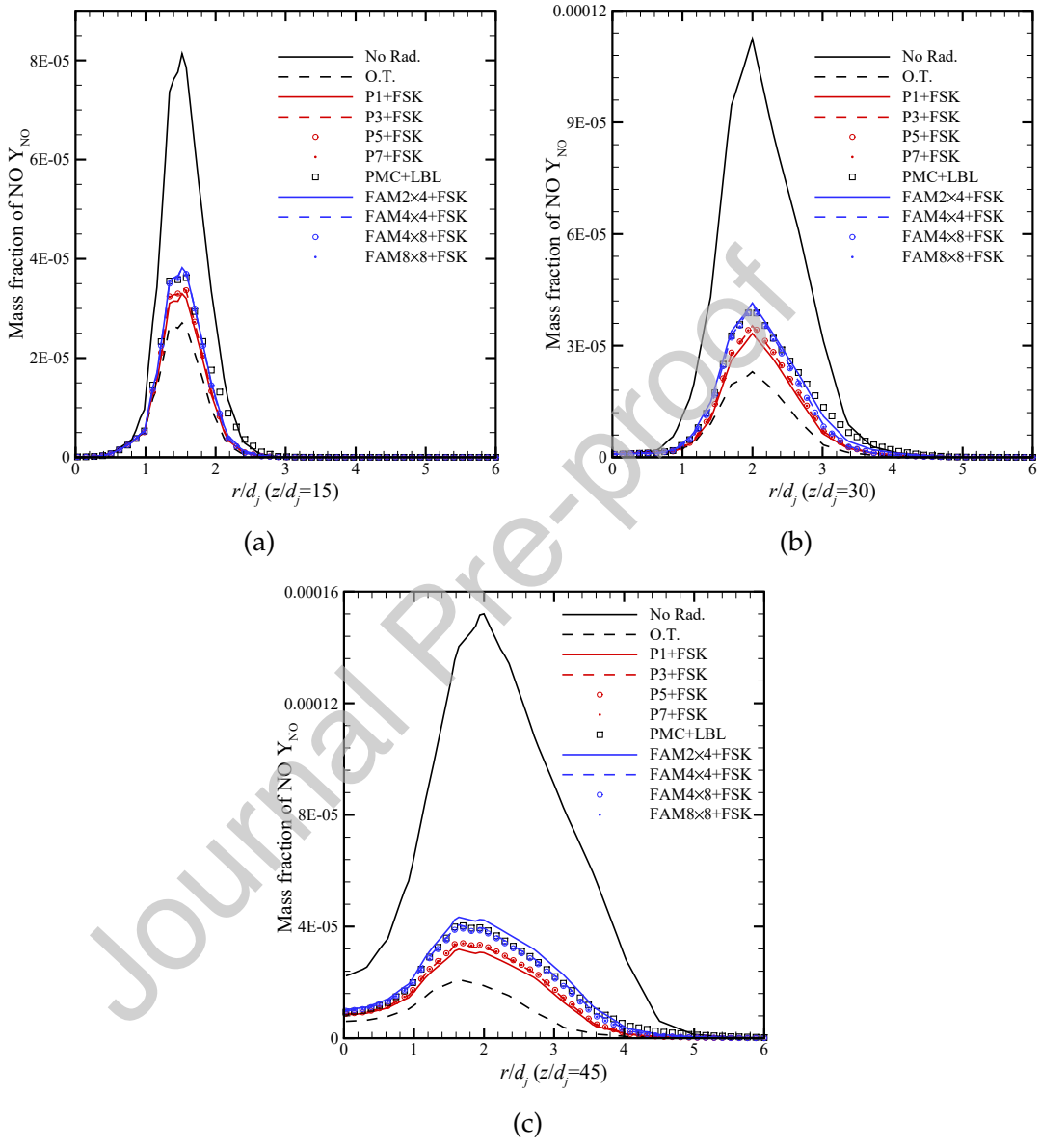

Figure 12: Mass fraction of NO profiles at different axial locations: (a) $z/d_j = 15$, (b) $z/d_j = 30$ and (c) $z/d_j = 45$.

Table 4: The heat release rate from combustion $\dot{Q}_C$, total emission $\dot{Q}_{rad}$, net radiative heat loss $\dot{Q}_{rad}$, radiation escape ratio as $\dot{Q}_{rad}/\dot{Q}_{emi}$ and actual radiant fraction $\chi_R = \dot{Q}_{rad}/\dot{Q}_C$ from different radiation solvers

Radiation Solver	$\dot{Q}_C$ (kW)	$\dot{Q}_{emi}$ (kW)	$\dot{Q}_{rad}$ (kW)	$\dot{Q}_{rad}/\dot{Q}_{emi}$	χ_R
No Rad	68.4	/	/	/	/
OT	66.6	40.7	40.7	100 %	61.1 %
P1+FSK	67.3	54.4	22.5	36.7 %	33.4%
P3+FSK	67.3	63.4	20.8	32.8 %	30.9%
P5+FSK	67.3	63.7	20.7	32.4%	30.7%
P7+FSK	67.3	63.8	20.6	32.2%	30.6%
FAM 2×4+FSK	66.6	73.8	17.7	24.0 %	32.0 %
FAM 4×4+FSK	67.0	69.8	17.2	24.7 %	26.6 %
FAM 4×8+FSK	67.0	68.0	18.6	27.4 %	25.8 %
FAM 8×8+FSK	67.0	67.7	18.7	27.7 %	27.8 %
PMC+LBL	67.3	71.3	21.6	30.2 %	28.0 %

The global energy budget of the flame is examined to further study the effects of radiation predicted by different RTE solvers. Several quantities that describe the overall heat transfer are shown in Table 4. The first quantity of interest is the actual total heat release rate from combustion, $\dot{Q}_C$. If the combustion is complete, $\dot{Q}_C$ should equal to the chemical energy that is supplied to the flame in the reactants, which are quantified by $\dot{m}_F \Delta h_C$, where $\dot{m}_F$ is the mass flow rate of the fuel and Δh_C is the lower heating value of the fuel. For Sandia Flame D×4, $\dot{m}_F \Delta H_C = 70.4$ kW and the rate of incoming enthalpy from the hot pilot is around 6% of that. Two quantities related to radiative transfer are the total emission $\dot{Q}_{emi}$ and the net radiative heat loss $\dot{Q}_{rad}$. The total emission $\dot{Q}_{emi}$ and the net radiative heat loss $\dot{Q}_{rad}$ are defined as the integral of the radiative emission S_{emi} and negative radiative heat source $-S_{rad}$ over the control volume, respectively. In terms of these three quantities, the radiant fraction χ_R is defined here as the ratio of $\dot{Q}_{rad}/\dot{Q}_C$ (instead of $\dot{Q}_{rad}/\dot{m}_F \Delta H_C$) and the radiation escape ratio as $\dot{Q}_{rad}/\dot{Q}_{emi}$. The radiant fraction χ_R is a useful notion to quantify the ratio of the net radiative energy that escapes to the surroundings to the chemical energy released from the combustion and the radiation escape ratio shows the ratio of escaped radiation to the emitted.

These quantities lead to better understanding of the role of radiative transfer on the combustion process. In addition to the direct cooling effects of radiation discussed ear-

lier, adding radiation is shown to have slightly lowered the total heat release rate from combustion $\dot{Q}_C$ as a secondary effect resulting in less complete combustion. Total radiative emission is found to be quite large, which is very close to the total heat release from combustion with the exception of OT. However, more than two-thirds of the emitted radiation gets reabsorbed in the flame indicating significant heat redistribution via radiation. Comparing global effects from different RTE solvers, as the order of P_N and the number of angles in FAM increase, both $\dot{Q}_{rad}/\dot{Q}_{emi}$ and radiant fraction χ_R approach the LBL-PMC solution. P_N appear to predict slightly higher $\dot{Q}_{rad}/\dot{Q}_{emi}$ and χ_R than the FAM solvers, which are consistent with the lower temperatures predicted by the P_N shown in this section.

Table 5 summarizes the computational time for both the reacting flow and the radiation evaluations including spectral models and RTE solvers. The first column shows the average total CPU time per time step for reacting flow including the radiation evaluation. For the P_N/FAM+FSK solvers, since radiation is evaluated once per 1/10/100/250 time steps, the times are collected from each one of the frequency schemes. In the second and third columns, the average $t_{RTE} + t_{overhead}$ and t_{FSK} are shown for runs with radiation evaluated once per time step only. The number of second-order elliptic PDEs for the corresponding P_N methods, the number of first-order PDEs for the corresponding FAM solvers and the number of photon bundles traced for the PMC method are also presented in the table.

Two empirical correlations can be obtained for the time cost of the P_N methods and the FAM for the simulations in which the radiation is evaluated in every time step,

$$t_{PN} = 0.0059 \times n_{quad} \times n_{PDE} + t_{flow} + t_{FSK} + t_{overhead,PN} \tag{15}$$

$$t_{FAM} = 0.0015 \times n_{quad} \times n_{PDE} + t_{flow} + t_{FSK} + t_{overhead,FAM} \tag{16}$$

where n_{quad} is the number of quadrature points for FSK (8 for the above simulations); n_{PDE} is the number of PDEs for the corresponding RTE method; $t_{flow} = 0.82$ s, $t_{FSK} = 0.06$ s, $t_{overhead,PN} = 0.07$ s and $t_{overhead,FAM} = 0.14$ s. It can be seen that by storing intensity coefficients I_n^m for each time step in coupled simulations, the time cost for different orders of P_N

Table 5: Average CPU time (including flow, chemistry and radiation calculation) per time step (radiation is evaluated once per 1/10/100/250 time steps for the P_N/FAM+FSK solvers and the average $t_{RTE} + t_{overhead}$ and t_{FSK} are only shown for runs with radiation evaluated every time step)

Radiation Solver	Average CPU Time (s)	t_{RTE}+$t_{overhead}$ (s)	t_{FSK} (s)	
No Rad	0.82	/	/	
PMC+LBL	0.87	/	/	5,000 with time-blending
PMC+LBL	0.92	/	/	10,000 with time-blending
	Radiation evaluation freq 1/10/100/250			
P1+FSK	0.97/0.85/0.82/0.82	0.09	0.06	1 second-order PDE
P3+FSK	1.05/0.87/0.83/0.83	0.17		4 second-order PDE
P5+FSK	1.36/0.88/0.84/0.84	0.48		9 second-order PDE
P7+FSK	1.64/0.90/0.85/0.85	0.76		16 second-order PDE
FAM 2×4+FSK	1.11/0.86/0.85/0.84	0.23		8 first-order PDE
FAM 4×4+FSK	1.20/0.87/0.85/0.84	0.32		16 first-order PDE
FAM 4×8+FSK	1.42/0.91/0.86/0.86	0.54		32 first-order PDE
FAM 8×8+FSK	1.78/0.94/0.87/0.87	0.9		64 first-order PDE

methods is actually linearly proportional to the number of the second-order PDEs of the P_N formulation with order N. In principle and especially for this flame, FAM formulation results in a system of uncoupled PDEs so that the benefit of storing intensities along each discrete ordinate is limited.

The leftmost number in the first column of Table 5 (corresponding to radiation evaluation frequency of 1) for the deterministic solvers represents the most expensive option regarding solution time. The time reported in the first row (0.82 s) is without any radiation calculation, i.e., only for flow and chemistry calculations. With their highest orders, which are P_7 and FAM 8×8, solving the RTE at every time step means the cost of radiation calculation ($t_{RTE} + t_{Overhead} + t_{FSK}$) is equal or greater than the solution of the flow and chemistry equations (P_7: 0.82 s, FAM 8×8: 0.96 s). Reducing the radiation evaluation frequency for the P_N/FAM+FSK solvers (or applying time blending for the case of PMC+LBL) are shown to be able to significantly reduce the overall time cost and make radiation evaluation relatively cheap compared to the computational cost of reacting flow simulations. For example, if P_7 is evaluated at every 100 time steps, the average cost of the radiation-coupled simulation is comparable to the no-radiation simulation. Since the computational cost of PMC+LBL solver is proportional to the total number of photon bundles traced for the

same mesh, it is not surprising that the time cost of PMC+LBL is small after applying the time-blending scheme. Both reducing solving frequency for the deterministic solvers and the time-blending scheme for PMC only work for pseudo-steady-state solutions or in transient solutions when the time step is extremely small compared to the time scale of flow. Usually the PMC is much more expensive compared to the deterministic solvers as a large number of photon bundles are needed for each time step for an acceptable statistical error. The surprisingly high computational efficiency of PMC+LBL in this particular case is due to several factors. The most important factor is time-blending. Since this flame is a stationary steady flame, this makes aggressive time-blending possible. In principle, by time-blending we are making an assumption that the changes in the scalar field relevant for radiation calculation are very small over many time steps. Other factors, such as optical thickness, importance sampling strategies, and mesh sizes, are also affecting the performance comparisons between deterministic solvers and the PMC+LBL solver. The implementation details of PMC are provided in the Appendix A.

4. Conclusion

In this work, we present a systematic comparison of several orders of P_N and DOM (FAM formulation) in 1D homogeneous configuration and in radiation-coupled reacting flow simulation of a turbulent jet flame. The 1D homogeneous case was simulated for four optical thicknesses ($\tau = 10, 1, 0.5, 0.001$). The findings from the homogeneous configurations are as follows.

- In 1-D cases homogeneous cases, both low-order P_N and FAM (except for $n_\theta = 2$) performs well in optically thick ($\tau = 10$) situation, where the radiative intensity is almost isotropic.

- For optically thin ($\tau = 0.001$) homogeneous case, both P_N and FAM have noticeable relative errors in the prediction of the incident radiation. However, FAM's results

improve much faster with the increase of discrete polar angles than that of P_N with the increase of order.

- If the homogeneous case is optically medium thick ($\tau = 1,\ 0.5$), both P_N and FAM approaches the exact solution with increase in order or polar angles. In these cases, lower order P_N performs better than lower order FAM. However, FAM results improve faster than P_N with increase in respective order and higher order FAM performs better than higher order P_N.

- As the optical thickness decreases, the solvers' capability to capture the anisotropic intensity profile reduces. Furthermore, P_N solvers introduces oscillations in the angular intensity profile at high orders.

A scaled Sandia D flame (Sandia D×4) was used as the target turbulent jet flame for radiation-coupled simulations. In these simulations the P_N and FAM solvers were used with FSK spectral model and the results were compared with an OT model and a PMC+LBL model. The key takeaway of the study are as follows.

- OT and no-radiation provides grossly inaccurate temperature distribution.

- The choice of RTE solver (and the order of RTE solver) noticeably changes the temperature distribution. FAM is more accurate than P_N in this axi-symmetric flame simulation.

- When compared with the radiant fraction from PMC+LBL simulation, P_N+FSK leads to a higher value while FAM+FSK leads to a lower value.

- The use of an intermittent evaluation of radiation by P_N and FAM and the use time-blending scheme for PMC+LBL can significantly accelerate radiation calculation without affecting accuracy.

Acknowledgement

This research was supported by National Science Foundation and the Department of Energy through Grant No. NSF1258635 (WG, MFM, SR), and by the National Science Foundation under Grant No. 1756005 (CD, SR). WG and RS acknowledge the support from the Exascale Computing Project (17-SC-20-SC), a collaborative effort of the U.S. Department of Energy Office of Science and the National Nuclear Security Administration.

Supplementary Materials

Supplementary material associated with this article can be found in the online version.

Declaration of Competing Interest

The authors declare that they have no known competing financial interests or personal relationships that could have appeared to influence the work reported in this paper.

References

[1] M. F. Modest, D. C. Haworth, Radiative Heat Transfer in Turbulent Combustion Systems, Springer Verlag, New York, 2016.

[2] F. Liu, J. L. Consalvi, P. J. Coelho, F. André, M. Gu, V. Solovjov, B. Webb, The impact of radiative heat transfer in combustion processes and its modeling–with a focus on turbulent flames, Fuel 281 (2020) 118555.

[3] G. Nathan, P. Kalt, Z. Alwahabi, B. Dally, P. Medwell, Q. Chan, Recent advances in the measurement of strongly radiating, turbulent reacting flows, Prog. Energy Combust. Sci. 38 (1) (2012) 41–61.

[4] A. Gunnarsson, K. Andersson, B. R. Adams, C. Fredriksson, Full-scale 3D-modelling of the radiative heat transfer in rotary kilns with a present bed material, Int. J. Heat Mass Transf. 147 (2020) 118924.

[5] H. Y. Wang, W. H. Chen, C. K. Law, Extinction of counterflow diffusion flames with radiative heat loss and nonunity Lewis numbers, Combust. Flame 148 (3) (2007) 100–116.

[6] J. Jayachandran, R. Zhao, F. N. Egolfopoulos, Determination of laminar flame speeds using stagnation and spherically expanding flames: Molecular transport and radiation effects, Combust. Flame 161 (9) (2014) 2305–2316.

[7] F. Liu, H. Guo, G. J. Smallwood, Effects of radiation model on the modeling of a laminar coflow methane/air diffusion flame, Combust. Flame 138 (1) (2004) 136–154.

[8] H. Guo, G. J. Smallwood, The interaction between soot and NO formation in a laminar axisymmetric coflow ethylene/air diffusion flame, Combust. Flame 149 (1) (2007) 225–233.

[9] P. J. Coelho, Numerical simulation of the interaction between turbulence and radiation in reactive flows, Prog. Energy Combust. Sci. 33 (4) (2007) 311–383.

[10] G. C. Fraga, P. J. Coelho, A. P. Petry, F. H. França, Investigation of the role of turbulent fluctuations on the time-averaged radiative emission in large-scale, turbulent pool fires, Fire Saf. J. 112 (2020) 102945.

[11] J. R. Howell, M. P. Mengüç, Challenges for radiative transfer 1: towards the effective solution of conjugate heat transfer problems, J. Quant. Spectrosc. Radiat. Transf. 221 (2018) 253–259.

[12] M. F. Modest, S. Mazumder, Radiative Heat Transfer, 4th Edition, Academic Press, New York, 2022.

[13] V. P. Solovjov, B. W. Webb, F. Andre, Radiative properties of gases, in: F. A. Kulacki (Ed.), Handbook of Thermal Science and Engineering, Springer International Publishing, Cham, 2017.

[14] C. Wang, M. F. Modest, T. Ren, J. Cai, B. He, Comparison and refinement of the various full-spectrum k-distribution and spectral line weighted-sum-of-gray-gases models for nonhomogeneous media, J. Quant. Spectrosc. Radiat. Transf. 271 (2021) 107695.

[15] M. Galtier, W. Woelffel, F. André, V. Solovjov, B. Webb, S. Roy, Assessment of narrow-band and full spectrum gas radiation methods in a real industrial glass furnace configuration, Appl. Therm. Eng. (2022) 119020.

[16] J. H. Jeans, The equations of radiative transfer of energy, Mon. Notices Royal Astron. Soc. 78 (1917) 28–36.

[17] R. L. Murray, Nuclear Reactor Physics, Prentice Hall, Englewood Cliffs, NJ, 1957.

[18] B. Davison, Neutron Transport Theory, Oxford University Press, London, 1958.

[19] J. C. Mark, The spherical harmonics method, Part I, Tech. Rep. Atomic Energy Report No. MT 92, National Research Council of Canada (1944).

[20] J. C. Mark, The spherical harmonics method, Part II, Tech. Rep. Atomic Energy Report No. MT 97, National Research Council of Canada (1945).

[21] R. E. Marshak, Note on the spherical harmonics method as applied to the Milne problem for a sphere, Phys. Rev. 71 (1947) 443–446.

[22] V. S. Arpaci, D. Gozum, Thermal stability of radiating fluids: the Bénard problem, Phys. Fluids 16 (5) (1973) 581–588.

[23] J. K. D. Higenyi, Higher order differential approximation of radiative energy transfer in a cylindrical gray medium, Ph.D. thesis, Rice University (1980).

[24] R. G. McClarren, C. D. Hauck, Robust and accurate filtered spherical harmonics expansions for radiative transfer, J. Comput. Phys. 229 (16) (2010) 5597–5614.

[25] P. Cheng, Dynamics of a radiating gas with application to flow over a wavy wall, AIAA J. 4 (2) (1966) 238–245.

[26] A. C. Ratzel, J. R. Howell, Two-dimensional radiation in absorbing–emitting–scattering media using the P-N approximation, ASME J. Heat Transf. 105 (1983) 333–340.

[27] M. P. Mengüç, R. Viskanta, Radiative transfer in three-dimensional rectangular enclosures containing inhomogeneous, anisotropically scattering media, J. Quant. Spectrosc. Radiat. Transf. 33 (6) (1985) 533–549.

[28] M. P. Mengüç, R. Viskanta, Radiative transfer in axisymmetric, finite cylindrical enclosures, ASME J. Heat Transf. 108 (1986) 271–276.

[29] A. K. Ziver, A. J. H. Goddard, A finite element method for multigroup diffusion-transport problems in two dimensions, Ann. Nucl. Energy 8 (11–12) (1981) 489–698.

[30] R. G. McClarren, T. M. Evans, R. B. Lowrie, J. D. Densmore, Semi-implicit time integration for pn thermal radiative transfer, J. Comput. Phys. 227 (16) (2008) 7561–7586.

[31] J. Yang, M. F. Modest, High-order *P-N* approximation for radiative transfer in arbitrary geometries, J. Quant. Spectrosc. Radiat. Transf. 104 (2) (2007) 217–227.

[32] M. F. Modest, J. Yang, Elliptic PDE formulation and boundary conditions of the spherical harmonics method of arbitrary order for general three-dimensional geometries, J. Quant. Spectrosc. Radiat. Transf. 109 (2008) 1641–1666.

[33] M. F. Modest, Further developments of the elliptic P_N-approximation formulation and its Marshak boundary conditions, Numer. Heat Transf. B: Fundam. 62 (2–3) (2012) 181–202.

[34] W. Ge, M. F. Modest, S. P. Roy, Development of high-order pn models for radiative heat transfer in special geometries and boundary conditions, J. Quant. Spectrosc. Radiat. Transf. 172 (2016) 98–109.

[35] W. Ge, R. Marquez, M. F. Modest, S. P. Roy, Implementation of high order spherical harmonics methods for radiative heat transfer on OpenFOAM, ASME J. Heat Transf. 137 (5) (2015) 052701.

[36] W. Ge, M. F. Modest, R. Marquez, Two-dimensional axisymmetric formulation of high order spherical harmonics methods for radiative heat transfer, J. Quant. Spectrosc. Radiat. Transf. 156 (2015) 58–66.

[37] S. Chandrasekhar, Radiative Transfer, Dover Publications, New York, 1960.

[38] K. D. Lathrop, Use of discrete-ordinate methods for solution of photon transport problems, Nucl. Sci. Eng. 24 (1966) 381–388.

[39] H. C. Hottel, A. F. Sarofim, L. B. Evans, I. A. Vasalos, Radiative transfer in anisotropically scattering media: Allowance for Fresnel reflection at the boundaries, ASME J. Heat Transf. 90 (1968) 56–62.

[40] J. S. Truelove, Three-dimensional radiation in absorbing–emitting–scattering media using the discrete-ordinates approximation, J. Quant. Spectrosc. Radiat. Transf. 39 (1) (1988) 27–31.

[41] W. A. Fiveland, A. S. Jamaluddin, Three-dimensional spectral radiative heat transfer solutions by the discrete-ordinates method, J. Thermophys. Heat Transf. 5 (3) (1991) 335–339.

[42] G. D. Raithby, E. H. Chui, A finite-volume method for predicting a radiant heat transfer enclosures with participating media, ASME J. Heat Transf. 112 (2) (1990) 415–423.

[43] E. H. Chui, G. D. Raithby, P. M. J. Hughes, Prediction of radiative transfer in cylindrical enclosures with the finite volume method, J. Thermophys. Heat Transf. 6 (4) (1992) 605–611.

[44] J. C. Chai, G. Parthasarathy, H. S. Lee, S. V. Patankar, Finite volume method radiative heat transfer procedure for irregular geometries, J. Thermophys. Heat Transf. 9 (3) (1995) 410–415.

[45] G. D. Raithby, Discussion of the finite-volume method for radiation, and its application using 3D unstructured meshes, Numer. Heat Transf. B: Fundam. 35 (4) (1999) 389–405.

[46] J. Y. Murthy, S. R. Mathur, Finite volume method for radiative heat transfer using unstructured meshes, J. Thermophys. Heat Transf. 12 (3) (1998) 313–321.

[47] M. Sankar, S. Mazumder, Solution of the radiative transfer equation in three-dimensional participating media using a hybrid discrete ordinates: Spherical harmonics method, ASME J. Heat Transf. 134 (11) (2012) 112702.

[48] A. R. Martin, C. Saltiel, J. C. Chai, W. Shyy, Convective and radiative internal heat transfer augmentation with fiber arrays, International Journal of Heat and Mass Transfer 41 (1998) 3431–3440.

[49] Y. Sun, X. Zhang, J. R. Howell, Evaluation of three different radiative transfer equation solvers for combined conduction and radiation heat transfer, J. Quant. Spectrosc. Radiat. Transf. 184 (2016) 262–273.

[50] J. Liu, H. M. Shang, Y. S. Chen, T. S. Wang, Analysis of discrete ordinates method with even parity formulation, J. Thermophys. Heat Transf. 11 (2) (1997) 253–260.

[51] W. A. Fiveland, J. P. Jessee, Comparison of discrete ordinates formulations for radiative heat transfer in multidimensional geometries, J. Thermophys. Heat Transf. 9 (1) (1995) 47–54.

[52] S. H. Kim, K. Y. Huh, Assessment of the finite-volume method and the discrete ordinate method for radiative heat transfer in a three-dimensional rectangular enclosure, Numer. Heat Transf. B: Fundam. 35 (1) (1999) 85–112.

[53] F. C. Lockwood, N. G. Shah, A new radiation solution method for incorporation in general combustion prediction procedures, Symp. (Int.) Combust. 18 (1981) 1405–1414.

[54] P. J. Coelho, J. Gonçalves, M. G. Carvalho, Modelling of radiative heat transfer in enclosures with obstacles, International Journal of Heat and Mass Transfer 41 (4) (1998) 745–756.

[55] N. Selçuk, N. Kayakol, Evaluation of discrete ordinates method for radiative transfer in rectangular furnaces, International Journal of Heat and Mass Transfer 40 (2) (1997) 213–222.

[56] S. C. Mishra, P. Chugh, P. Kumar, K. Mitra, Development and comparison of the DTM, the DOM and the FVM formulations for the short-pulse laser transport through a participating medium, Int. J. Heat Mass Transf. 49 (11-12) (2006) 1820–1832.

[57] M. Frank, M. Seaid, A. Klar, R. Pinnau, G. Thömmes, J. Janicka, A comparison of approximate models for radiation in gas turbines, Prog. Comput. Fluid Dyn. 4 (2004) 191–197.

[58] E. W. Larsen, G. Thömmes, A. Klar, M. Seaıd̈, T. Götz, Simplified PN approximations to the equations of radiative heat transfer and applications, J. Comput. Phys. 183 (2) (2002) 652–675.

[59] A. Habibi, B. Merci, G. Heynderickx, Impact of radiation models in CFD simulations of steam cracking furnaces, Comput. Chem. Eng. 31 (11) (2007) 1389–1406.

[60] S. P. Roy, J. Cai, W. Ge, M. Modest, Computational cost and accuracy comparison of radiation solvers with emphasis on combustion simulations, in: Proceedings of CHT-15. 6th Int. Symp. on Adv. in Comput. Heat Transf., Piscataway, NJ, 2015.

[61] C. David, W. Ge, S. P. Roy, M. Modest, R. Sankaran, Comparison of radiation models for a turbulent piloted methane/air jet flame: A frozen-field study, in: Proceedings of the ASME 2021 Summer Heat Transf. Conf., Virutal, 2021, Paper no. SHTC2021–62417.

[62] C. Wang, W. Ge, M. F. Modest, J. Cai, A full-spectrum k-distribution look-up table for radiative transfer in nonhomogeneous gaseous media, J. Quant. Spectrosc. Radiat. Transf. 168 (2016) 45–56.

[63] T. M. MacRobert, Spherical Harmonics, 3rd Edition, Pergamon Press, New York, 1967.

[64] J. Y. Murthy, S. R. Mathur, Radiative heat transfer in axisymmetric geometries using an unstructured finite-volume method, Numer. Heat Transf. B: Fundam. 33 (4) (1998) 397–416.

[65] J. Cai, S. Roy, M. F. Modest, A comparison of specularly reflective boundary conditions and rotationally invariant formulations for Discrete Ordinate Methods in axisymmetric geometries, J. Quant. Spectrosc. Radiat. Transf. 182 (2016) 75–86.

[66] L. S. Rothman, I. E. Gordon, R. J. Barber, H. Dothe, R. R. Gamache, A. Goldman, V. I. Perevalov, S. A. Tashkun, J. Tennyson, HITEMP, the high-temperature molecular spectroscopic database, J. Quant. Spectrosc. Radiat. Transf. 111 (15) (2010) 2139–2150.

[67] L. S. Rothman, I. E. Gordon, Y. Babikov, A. Barbe, D. Chris Benner, P. F. Bernath, M. Birk, L. Bizzocchi, V. Boudon, L. R. Brown, A. Campargue, K. Chance, E. A. Cohen, L. H. Coudert, V. M. Devi, B. J. Drouin, A. Fayt, J.-M. Flaud, R. R. Gamache, J. J. Harrison, J.-M. Hartmann, C. Hill, J. T. Hodges, D. Jacquemart, A. Jolly, J. Lamouroux, R. J. Le Roy, G. Li, D. A. Long, O. M. Lyulin, C. J. Mackie, S. T. Massie, S. Mikhailenko, H. S. P. Müller, O. V. Naumenko, A. V. Nikitin, J. Orphal, V. Perevalov, A. Perrin, E. R.

Polovtseva, C. Richard, M. A. H. Smith, E. Starikova, K. Sung, S. Tashkun, J. Tennyson, G. C. Toon, Vl. G. Tyuterev, G. Wagner, The HITRAN2012 molecular spectroscopic database, J. Quant. Spectrosc. Radiat. Transf. 130 (2013) 4–50.

[68] T. Ren, M. F. Modest, Line-by-Line Random-Number Database for Monte Carlo Simulations of Radiation in Combustion System, ASME J. Heat Transf. 141.

[69] A. Soufiani, J. Taine, High temperature gas radiative property parameters of statistical narrow-band model for H_2O, CO_2 and CO, and correlated-*k* model for H_2O and CO_2, Int. J. Heat Mass Transf. 40 (4) (1997) 987–991.

[70] A. Wang, M. F. Modest, High-accuracy, compact database of narrow-band *k*-distributions for water vapor and carbon dioxide, in: M. P. Mengüç, N. Selçuk (Eds.), Proc. of the ICHMT 4th Int. Symp. on Radiat. Transf., Istanbul, Turkey, 2004.

[71] O. Marin, R. O. Buckius, A model of the cumulative distribution function for wide band radiative properties, J. Quant. Spectrosc. Radiat. Transf. 59 (1998) 671–685.

[72] M. F. Modest, H. Zhang, The full-spectrum correlated-k distribution for thermal radiation from molecular gas-particulate mixtures, ASME J. Heat Transf. 124 (1) (2002) 30–38.

[73] J. Cai, M. F. Modest, Improved full-spectrum k-distribution implementation for inhomogeneous media using a narrow-band database, J. of Quant. Spectrosc. and Radiat. Transf. 141 (2014) 65–72.

[74] V. P. Solovjov, B. W. Webb, F. Andre, The rank correlated fsk model for prediction of gas radiation in non-uniform media, and its relationship to the rank correlated slw model, J. of Quant. Spectrosc. and Radiat. Transf. 214 (2018) 120–132.

[75] A. Bansal, M. Modest, D. Levin, Multigroup correlated-k distribution method for nonequilibrium atomic radiation, J. of Quant. Spectrosc. and Radiat. Transf. 24 (3) (2010) 638–646.

[76] M. F. Modest, R. J. Riazzi, Assembly of full-spectrum k-distributions from a narrow-band database; effects of mixing gases, gases and nongray absorbing particles, and mixtures with nongray scatterers in nongray enclosures, J. of Quant. Spectrosc. and Radiat. Transf. 90 (2) (2005) 169–189.

[77] R. S. Barlow, J. H. Frank, Effects of turbulence on species mass fractions in methane/air jet flames, Symp. (Int.) Combust. 27 (1998) 1087–1095.

[78] G. Li, M. F. Modest, Application of composition PDF methods in the investigation of turbulence–radiation interactions, J. Quant. Spectrosc. Radiat. Transf. 73 (2–5) (2002) 461–472.

[79] G. Pal, A. Gupta, M. F. Modest, D. C. Haworth, Comparison of accuracy and computational expense of radiation models in simulation of nonpremixed turbulent jet flames, Combustion and Flame 162 (6).

[80] J. H. Ferziger, M. Peric, Computational Methods for Fluid Dynamics, 3rd Edition, Springer, Berlin, 2012.

[81] C. T. Bowman, R. K. Hanson, W. C. Gardiner, V. Lissianski, G. P. Smith, D. M. Golden, M. Frenklach, B. Eiteneer, M. Goldenberg, GRI-mech 2.21 (1995).

[82] W. H. Press, S. A. Teukolsky, W. T. Vetterling, B. P. Flannery, Numerical Recipes – The Art of Scientific Computing, 3rd Edition, Cambridge University Press, Cambridge, 2007.

[83] A. Karlsson, Modeling auto-ignition, flame propagation and combustion in non-stationary turbulent sprays, Ph.D. thesis, Chalmers University of Technology (1995).

[84] T. Ren, M. F. Modest, Hybrid wavenumber selection scheme for line-by-line photon Monte Carlo simulations in high-temperature gases, Journal of Heat Transfer 135 (8) (2013) 084501.

[85] J. Farmer, S. Roy, A quasi-Monte Carlo solver for thermal radiation in participating media, Journal of Quantiative and spectroscopic Radiative Transfer 242 (2020) 106753.

Appendix A. Some discussions on the photon Monte Carlo method

The photon Monte Carlo (PMC) method accounts for the radiative transport by emitting and tracing a statistically meaningful sample of representative photons bundles or rays. For this discussion, let's consider a ray denoted by its index j. Then the ray's origin (x_j^i, y_j^i, z_j^i), direction (θ_j, ϕ_j), the wavenumber (η_j), and initial energy content E_j^{i0} together completely define the ray. Here the superscript i denotes the index of the finite volume computational cell within which the origin point is located indicating that the point (x_j^i, y_j^i, z_j^i) is located within the extent of the finite volume cell i. The origin and the direction are determined from independent random numbers as discussed in [12]. The wavenumber of the ray is obtained using another random number as discussed in [84]. The energy content of the ray E_j^{i0} is calculated from the emissive power of the computational cell from which the ray originated (i.e., cell i). If the emissive power of cell i is $\mathbb{E}_i$, then the initial energy of ray j, which originated from cell i, is given by $E_j^{i0} = \frac{\mathbb{E}_i}{n_i}$, where n_i is the total number of rays emitted from the cell i. The number of rays to be emitted from each cell (n_i) is determined from distribution of the emissive power such that the higher the emissive power of the cell, the more rays it will emit. This ensures that the energy content of the rays are similar to one another making each ray statistically equivalent to one another. This "adaptive emission" approach makes the scheme statistically more efficient and has been discussed in detail in [12] and in [85]. As the ray travels through the computational mesh, its energy is attenuated due to absorption. As a ray of wavenumber η_j containing energy E_j^k enters cell k and passes an optical distance τ_η^k inside cell k, its energy reduces to $E_j^k e^{-\tau_\eta^k}$ as it deposits an amount of energy $\Delta E_j^k = E_j^k(1 - e^{-\tau_\eta^k})$ in to the cell. The ray is traced until all its energy is attenuated completely or it moves outside the computational domain. The radiative source term for the medium is then determined by keeping track of the energy deposition and emission in each computational cell.

At each time step, a total of N_r rays are emitted and tracked. The N_r rays are organized into n_s complete statistical sets such that, $N_r = n_s \times n_r$. Here n_r is the number of rays emitted, per statistical set, from the entire domain such that $n_r = \sum_i n_i$ and $\mathbb{E}_{total} = \sum_{j \in n_r} E_j^{i0}$, where $\mathbb{E}_{total}$ is the total emissive power of the entire domain, i.e., $\mathbb{E}_{total} = \sum_i \mathbb{E}_i$. Every statistical set, i.e., n_r rays, produces one solution of the radiative transport in the entire field. Therefore, every time step one obtains n_s independent solutions of the radiation field, which are then averaged to find the radiation field for that time step. As per the time-blending scheme presented in Eq. (14), this averaged radiation field is then blended with previous solutions before being fed back to the energy conservation equation (Eq. (1)).

Declaration of interests

☒ The authors declare that they have no known competing financial interests or personal relationships that could have appeared to influence the work reported in this paper.

☐ The authors declare the following financial interests/personal relationships which may be considered as potential competing interests:

Wenjun Ge: Conceptualization, Methodology, Software, Validation, Visualization, Writing

David Chloe: Validation

Michael Modest: Supervision, Funding acquisition

Ramanan Sankaran: Funding acquisition

Somesh Roy: Conceptualization, Methodology, Software, Validation, Visualization, Writing, Supervision, Funding acquisition